Structural and Electronic Properties of TiO_2, IrO_2, and SnO_2 for Photocatalysis and Photovoltaics

by

Naija Pison

December 20, 2024

Supervisor: Prof. Eleonora Luppi

Laboratoire de Chimie Théorique Sorbonne Université, Paris, France

This master's thesis is submitted to East African Institute for Fundamental Research (ICTP-EAIFR) for partial fulfillment of the requirement of Master's Degree in Physics.

United Nations Educational, Scientific and Cultural Organization

ICTP - East African Institute for Fundamental Research under the auspices of UNESCO

Declaration

I, **Mr.Naija Pison**, hereby declare that this thesis entitled, *"Structural and Electronic Properties of TiO_2, IrO_2, and SnO_2 for Photocatalysis and Photovoltaics,"* is my own original work and has not been submitted for any degree or examination at any other university.
This work was conducted under the supervision of **Prof. Eleonora Luppi** at the Laboratoire de Chimie Théorique, Sorbonne Université, Paris, France.

Signed by the Candidate:

Signed by the Supervisor: 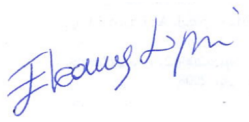

Dedication

This work is lovingly dedicated to my parents **Mr.Byeshamika Nathan** and **Mrs.Byeshamika Medius**, whose unwavering love and sacrifices have made this journey a possibility. You faced countless hardships, often going without, only to give me opportunities you never had, yet believed I deserved. Despite the weight of challenges and the lack of formal education, you labored tirelessly, determined to see me grow, learn, and achieve my dreams. Every achievement in these pages is a reflection of your strength, resilience, and boundless generosity. This work is my tribute to you, with all my love and gratitude, for you have been the quiet, steady foundation of my success. Your dreams live here, within every step of my journey.

Acknowledgement

First and foremost, I am deeply thankful to God Almighty for His guidance, strength, and countless blessings that have made this journey possible. His unwavering presence has been my source of hope and resilience throughout my studies.

I extend my sincere gratitude to my supervisor, Prof. Eleonora Luppi, at the Laboratoire de Chimie Théorique, Sorbonne Université-Paris. Her expertise, encouragement, and insightful guidance have been invaluable in shaping my research and helping me overcome the challenges I encountered. Her dedication and mentorship have greatly enriched my academic journey.

I am deeply grateful to the International Center for Theoretical Physics (ICTP) through the East African Institute for Fundemental Research (EAIFR) for giving me the opportunity to pursue my master's courses at the University of Rwanda.
I also thank The World Academy of Science (TWAS) for providing the scholarship grant.

Special thanks to Prof. Catherine Meriaux,acting Director of ICTP-EAIFR, for her exceptional leadership, guidance, and encouragement and in general to the entire staff for their commitment to fostering a supportive and stimulating environment for academic excellence.

My heartfelt thanks also go to my friends and classmates, whose support, encouragement, and shared experiences have made this journey both memorable and fulfilling. The discussions and motivation that we shared have played a pivotal role in my progress.

Finally, I am forever grateful to my family for their endless love, patience, and support. Your belief in me and your encouragement have been my constant motivation.

Thank you all for your contributions that have been instrumental in making this accomplishment a reality.May God bless you.

Abstract

This thesis investigates the electronic excitations of titanium dioxide (TiO_2), iridium dioxide (IrO_2), and tin dioxide (SnO_2), which are key materials for photocatalysis and photovoltaics. To perform this study, we used advanced computational methods, such as Density Functional Theory (DFT) and Green's function approach within the GW approximation.
We studied the rutile and anatase phases of TiO_2 and SnO_2, as well as the rutile phase of IrO_2 by calculating their electronic properties at the DFT level. For SnO_2, we went also beyond DFT by calculating quasiparticle excitations within the GW approximation, discussing the role of pseudopotential description.The exchange correlation function was described using the local density approximation (LDA) and the Perdew-Burke-Ernzerhof (PBE) which is one of the most commonly used parameterizations of the generalized gradient approximation (GGA).
The structural parameters of the dioxides are found to be in a fair agreement with the experimental values and previous calculations for all oxides. The band gaps obtained are also in fair agreement with the previous DFT calculations although there is still a big gap between the DFT band gap (E_{Gap}^{DFT}) and experimental gap. The self-consistent GW band gap (E_{Gap}^{GW}) for rutile SnO_2 *, i.e,* 3.81 is in better agreement with both previous studies and experiments *, i.e,* 3.56 compared to G_0W_0 band gap *, i.e,* 3.08.

Contents

List of Figures

List of Tables

Chapter 1

Introduction.

The escalating global demand for energy and the diverse environmental impacts of fossil fuel use have required a shift toward renewable and sustainable sources of energy. Fossil fuels, while currently are the dominant sources of energy, contribute significantly to environmental degradation through the release of greenhouse gases, leading to climate change and air pollution[1]. Renewable energy sources, such as solar and wind energy, offer a sustainable alternative that can help mitigate these adverse environmental effects and provide a more stable and secure energy for the future[2, 3]

The study of the electronic excitations of materials has become increasingly significant in the development of technologies for photocatalysis and photovoltaics. Among the various materials investigated, titanium dioxide (TiO_2), iridium dioxide (IrO_2) and tin dioxide (SnO_2) have received considerable attention due to their unique physical and chemical properties [4, 5, 6]. These materials exhibit exceptional stability, high refractive indices, and are capable of harnessing light energy for catalytic and photovoltaic applications [7, 8]. In order to fully utilize these materials for these applications, a deep understanding of their key bulk properties is therefore necessary.
This study aims to investigate the electronic structure of TiO_2, IrO_2, and SnO_2 in bulk form. We will employ density functional theory (DFT) and Green's function approach within the GW approximation to gain insight into the electronic structure and excitations of these materials.
DFT will allow us to determine the ground state electronic structure of TiO_2, IrO_2, and SnO_2, and the electronic band structure and hence the band gap. However, standard DFT calculations underestimate the band gap, which is a limitation that we address using the GW method.
GW, as a theory of many bodies perturbation, will be used to improve the accuracy of the electronic band gap obtained from the DFT calculation of SnO_2 by accounting for electron-electron interactions more precisely. The GW approach gives a more accurate description of electronic excitations, providing the quasiparticle energies. By applying GW, we aim to obtain a corrected band structure that better reflects the true excitations within these materials, which is essential for predicting their optical behavior in photocatalytic and photovoltaic applications.

1.1 Photocatalysis and Photovoltaics.

Photocatalysis involves the acceleration of a photoreaction in the presence of a catalyst. TiO_2, IrO_2, and SnO_2 are widely used as photocatalysts because of their ability to generate electron-hole pairs upon exposure to light, which can then participate in redox reactions. These properties are exploited in various applications, such as water splitting for hydrogen production, pollutant degradation, and sterilization processes [9, 10].
Photovoltaics, on the other hand, involve the conversion of light into electrical energy. Materials with suitable band gaps and efficient charge carrier dynamics are crucial for the development of high-efficiency solar cells. The ability of TiO_2, IrO_2, and SnO_2 to absorb sunlight and generate charge carriers makes them promising candidates for use in photovoltaic devices [5, 6].

1.2 Importance of TiO_2.

Even after half a century of research, the investigation of the fundamental properties of TiO_2 crystal phases remains important and fruitful [11, 12]. TiO_2 is one of the most studied materials for photocatalysis and photovoltaics due to its excellent properties. TiO_2 also has a high oxidizing power over similar materials as semiconductor photocatalyst. In pursuit of the development of renewable energy, it has become one of the most promising semiconducting photocatalysis materials.
All of these drive continuous and sustainable investigations on TiO_2 from various physical and chemical aspects. TiO_2 has three basic crystalline phases: brookite, anatase, and rutile, but the anatase and rutile phases are of great interest to us. It is chemically stable, non-toxic, and cost-effective[8]. It has a suitable band gap of 3.0-3.2 eV, [10, 12, 13, 14], which allows it to absorb ultraviolet light effectively. This makes TiO_2 ideal for applications in environmental cleanup and conversion of solar energy [10, 15]. However, for photocatalyst applications, the TiO_2 band gap is too big ($\sim$ 3.0 eV for the rutile phase and $\sim$ 3.2 eV for anatase phase)[12], while the preferred band gap should be $\sim$ 2.0 eV. Numerous investigations on this issue have been carried out [16].
In photocatalysis, TiO_2 is used for the degradation of organic pollutants and in water splitting reactions to produce hydrogen. Its high stability and strong oxidation power make it effective in these applications. For photovoltaics, TiO_2 is often used as a photoanode in dye-sensitized solar cells (DSSCs), where it facilitates the separation and transport of charge carriers generated by sunlight absorption [15].

1.3 Importance of IrO_2.

IrO_2 is known for its excellent catalytic properties, particularly in oxygen evolution reactions (OER). IrO_2 has a high work function and exhibits good electrical conductivity, which makes it suitable for use in electrochemical and photoelectrochemical cells [17].
In photocatalysis, IrO_2 is often used as a co-catalyst to improve the efficiency of water splitting reactions. Its ability to efficiently catalyze the OER makes it a critical component in systems designed for the production of hydrogen through water splitting. In photovoltaics, IrO_2 can be used to improve the stability and performance of photoelectrochemical cells, where it facilitates the separation of charge carriers and enhances overall cell efficiency [17].

1.4 Importance of SnO_2.

SnO_2 is another material of interest for photocatalysis and photovoltaics. SnO_2 has a wide band gap of about 3.6 eV, which makes it transparent to visible light and suitable for applications that require transparency and conductivity, such as in transparent conductive oxides (TCOs)[18].
In photocatalysis, SnO_2 is used in combination with other materials to enhance its photocatalytic activity. It serves as a support for other photocatalysts, improving their stability and efficiency. In photovoltaic applications, SnO_2 is used as a conductive layer in solar cells, where it helps to collect and transport electrons. Its high electron mobility and stability under UV light makes it a valuable material in these applications [18].

1.5 Optical Properties and Their Importance.

The optical properties of materials, including absorption, reflection, and refraction, are critical in determining their effectiveness in photocatalysis and photovoltaics. These properties are influenced by the electronic structure and excitations within the material. Understanding fundamental optical properties provides information on how these materials interact with light and how their performance can be optimized for specific applications[19].
For bulk systems, methods such as the GW approach and the Bethe-Salpeter equation (BSE) are employed to accurately describe electronic excitations and optical responses. These methods account for many-body interactions and provide a comprehensive understanding of the electronic structure and optical properties of the material[20, 21, 22, 23, 24, 25]

1.6 Research Objectives.

This research aims to provide a comprehensive understanding of the electronic properties of TiO_2, IrO_2, and SnO_2. The specific objectives are as follows:

1. Analyze the impact of pseudopotentials on accuracy.
2. Investigate the electronic structure of TiO_2, IrO_2, and SnO_2 using DFT.
3. Investigate the quasiparticle energies by applying the GW approximation to achieve a more accurate description of the electronic structure of SnO_2, analyzing variations due to different pseudopotentials, and comparing with experimental data and previous works.

1.7 Novelty and Contributions.

This research offers novel insights into the electronic excitations of TiO_2, IrO_2, and SnO_2 by combining advanced computational methods DFT and GW.
The main novelty and contribution of this study is **understanding of electronic structure and quasiparticle energies** by applying DFT in conjunction with the GW approximation. This work provides a detailed and comparative analysis of the electronic

structures of TiO_2, IrO_2, and SnO_2. The study explores the impact of different pseudopotentials on band gap predictions, helping to address discrepancies with experimental data, and contributing to more reliable models of these materials.

1.8 Mode of work and Challenges faced.

The successful completion of this thesis was achieved through a collaborative effort between my supervisor and myself, utilizing both independent work and guided mentorship. The following is a detailed account of our working mode, individual contributions, and the challenges faced during the study:

1.8.1 Mode of work.

- I researched and wrote the theoretical framework, focusing on the DFT and GW approximation under the guidance of my supervisor. This required a review of the extensive literature to establish a solid understanding of these methods and their applications to TiO_2, IrO_2, and SnO_2.
- All DFT calculations were performed using quantum espresso, ensuring the convergence of k-points and the cutoff energy. For SnO_2, I extended the analysis to GW calculations, troubleshooting differences arising from the use of standard and stringent pseudopotentials. This involved parameter optimization and interpreting unexpected results such as flat bands. I conducted structural optimizations, band structure analysis, and studies on electronic properties for all materials.
- The results were interpreted and compared with experimental data and previous studies to validate the findings. I wrote most of the thesis, detailing the computational details and results: my supervisor took the lead in the discussion section.
- My supervisor provided critical advice on the implementation of the GW. Her expertise helped address challenges in convergence tests and ensured an accurate representation of quasiparticle energies. She generated additional pseudopotentials when existing ones did not yield accurate results, particularly for SnO_2.
- She regularly reviewed my drafts, provided feedback to refine arguments, and ensured the alignment of the work with academic standards. Regular discussions clarified conceptual uncertainties and directed the research toward relevant objectives.
- During my visit to Sorbonne Université-Paris, France, she facilitated access to resources and arranged meetings to discuss advanced topics like the core correction mismatch,theory on GW, and pseudopotential validation.

1.8.2 Challenges.

- Being geographically distant for most of the project,it required innovative ways to ensure consistent progress and maintain close communication with my supervisor. Conducting remote discussions with my supervisor on WhatsApp was challenging due to unstable internet connections. This required asynchronous communication and flexible scheduling.

- Limited computational power occasionally delayed simulations, especially for GW calculations that require high precision. Efficient resource allocation and batch processing were essential to overcome this.
- The core correction issue in the Yambo code necessitated generating and validating new pseudopotentials, adding complexity to the study.
- Adapting to a new work environment during my visit to France was initially challenging but ultimately enriching for the research.

Chapter 2

Theory.

2.1 Introduction to DFT

DFT is a quantum mechanical method used to investigate the electronic structure of many-body systems, particularly atoms, molecules, and solids. It balances accuracy and computational efficiency, making it valuable in materials science, chemistry, and physics. The core idea of DFT is that the ground-state properties of a system of interacting electrons can be determined uniquely by the electron density alone, rather than by the many-body wavefunction. This simplifies the complex problem of solving the Schrödinger equation for many-electron systems.

2.1.1 The Hohenberg-Kohn Theorems.

The theoretical foundation of DFT is based on two key theorems proposed by Hohenberg and Kohn in 1964 [26] which are:

2.1.1.1 First Hohenberg-Kohn Theorem.

The first Hohenberg-Kohn theorem [26] states that the ground-state properties of a many-electron system are uniquely determined by the electron density $\rho(\mathbf{r})$. This implies that there exists a unique functional of the electron density, $E[\rho(\mathbf{r})]$, which gives the energy of the ground state when minimized.
Mathematically, this is expressed as:

$$E[\rho(\mathbf{r})] = T[\rho(\mathbf{r})] + V_{\text{ext}}[\rho(\mathbf{r})] + V_{\text{ee}}[\rho(\mathbf{r})], \tag{2.1.1}$$

where $T[\rho(\mathbf{r})]$ is the kinetic energy functional, $V_{\text{ext}}[\rho(\mathbf{r})]$ is the external potential energy functional, and $V_{\text{ee}}[\rho(\mathbf{r})]$ is the electron-electron interaction energy functional [27].

2.1.1.2 Second Hohenberg-Kohn Theorem.

The second Hohenberg-Kohn theorem [26] asserts that the electron density that minimizes the energy functional $E[\rho(\mathbf{r})]$ is the true ground-state electron density. Therefore, the ground-state energy can be obtained by minimizing the energy functional with respect to the electron density[27]:

$$\frac{\delta E[\rho(\mathbf{r})]}{\delta \rho(\mathbf{r})} = 0. \tag{2.1.2}$$

2.1.2 The Kohn-Sham Equations.

While the Hohenberg-Kohn theorems provide the conceptual framework for DFT, they do not provide a practical method to calculate the electron density. The Kohn-Sham approach, introduced by Kohn and Sham in 1965 [28], reformulates the many-body problem into a set of self-consistent single-particle equations. The goal is to minimize the unknown part of $E[\rho]$.
In the Kohn-Sham formalism, the interacting system of electrons is replaced by a fictitious system of non-interacting electrons that have the same electron density as the real system. The Kohn-Sham equations are:

$$\left[-\frac{1}{2}\nabla^2 + V_{\text{eff}}(\mathbf{r})\right]\psi_i^{\text{KS}}(\mathbf{r}) = \epsilon_i^{\text{KS}}\psi_i^{\text{KS}}(\mathbf{r}), \tag{2.1.3}$$

where $\psi_i^{\text{KS}}(\mathbf{r})$ are the Kohn-Sham orbitals, ϵ_i^{KS} are the Kohn-Sham eigenvalues, and $V_{\text{eff}}(\mathbf{r})$ is the effective potential given by:

$$V_{\text{eff}}(\mathbf{r}) = V_{\text{ext}}(\mathbf{r}) + \int \frac{\rho(\mathbf{r}')}{|\mathbf{r}-\mathbf{r}'|}d\mathbf{r}' + V_{\text{xc}}[\rho(\mathbf{r})]. \tag{2.1.4}$$

Here, $V_{\text{ext}}(\mathbf{r})$ is the external potential, the second term is the Hartree potential representing the classical electrostatic interaction, and $V_{\text{xc}}[\rho(\mathbf{r})]$ is the exchange-correlation potential[27, 28, 29, 30].

2.1.2.1 Exchange-Correlation Functional.

$V_{\text{xc}}[\rho(\mathbf{r})]$ accounts for the complex quantum-mechanical interactions between electrons. It includes both exchange interactions (which arise due to the Pauli exclusion principle) and correlation effects (which arise due to the dynamic correlations between electron motions).
The exact form of $V_{\text{xc}}[\rho(\mathbf{r})]$ is unknown and various approximations are used [30]:

Local Density Approximation (LDA): Assumes that the exchange-correlation energy at each point in space depends only on the electron density at that point. It is given by:

$$E_{\text{xc}}^{\text{LDA}}[\rho(\mathbf{r})] = \int \rho(\mathbf{r})\epsilon_{\text{xc}}[\rho(\mathbf{r})]d\mathbf{r}. \tag{2.1.5}$$

Generalized Gradient Approximation (GGA): Improves upon LDA by including the gradient of the electron density. The exchange-correlation energy in GGA is expressed as:

$$E_{\text{xc}}^{\text{GGA}}[\rho(\mathbf{r}), \nabla\rho(\mathbf{r})] = \int f(\rho(\mathbf{r}), \nabla\rho(\mathbf{r}))d\mathbf{r}. \tag{2.1.6}$$

In this study, we will use the Perdew-Burke-Ernzerhof (PBE) [31] form of GGA, chosen for its balance of computational efficiency and accuracy. In DFT, the accuracy of computed properties strongly depends on the choice of the exchange-correlation functional. PBE functional is one of the most commonly used parameterizations of GGA. It was designed to improve the LDA by including the gradient of the electron density, allowing it to better describe systems with inhomogeneous electron distributions.

The PBE functional modifies the exchange-correlation energy term by incorporating both the density $\rho(\mathbf{r})$ and its gradient $\nabla\rho(\mathbf{r})$. This extension provides a more accurate description of the spatial variation of the electron density, particularly important in complex materials such as TiO_2, IrO_2, and SnO_2, where the electron density varies significantly near atomic sites and between bonds. The PBE exchange-correlation energy $E_{\text{xc}}^{\text{PBE}}[\rho]$ can be expressed as:

$$E_{\text{xc}}^{\text{PBE}}[\rho] = \int \rho(\mathbf{r})\epsilon_{\text{xc}}^{\text{PBE}}(\rho, \nabla\rho)d\mathbf{r}, \tag{2.1.7}$$

where $\epsilon_{\text{xc}}^{\text{PBE}}(\rho, \nabla\rho)$ represents the exchange-correlation energy density.

Features of PBE Functional: The PBE functional is widely used due to its balance of computational efficiency and reasonable accuracy for a wide range of materials. Its design features include:

- Non-empirical Derivation: Unlike some GGA functionals that rely on empirical fitting to reproduce experimental data, PBE is derived based on fundamental principles. It satisfies several exact conditions known for the exchange-correlation functional, such as the correct asymptotic behavior and the gradient expansion for slowly varying densities.
- Improved Treatment of Bonds: The gradient correction of PBE allows it to better describe the bond lengths, binding energies, and the electronic structure of materials where the electron density is not uniform. This is particularly beneficial for transition metal oxides.
- Moderate Band Gap Improvement: Although PBE improves on LDA by yielding more accurate geometries and total energies, it still underestimates band gaps in semiconductors and insulators, similar to other GGAs. For applications requiring precise band gap predictions, PBE can serve as a starting point, with corrections applied through methods such as the GW approximation.

2.2 GW Approximation.

The GW approximation is a powerful and widely used method in condensed matter physics and quantum chemistry, primarily employed to improve the description of electronic excitations in materials. Introduced by Hedin in 1965 [20, 22, 25], this approach goes beyond mean field theories like DFT by incorporating many body effects, specifically through the calculation of self-energy operator Σ. The self-energy accounts for electron-electron interactions, providing a more accurate quasiparticle[1] energies which represent the energies of electrons as influenced by the surrounding electron environment.
In the GW formalism, the self-energy Σ is approximated as the product of the single particle Green's function G and the screened Coulomb interaction W, leading to:

[1] In the GW framework, a quasiparticle describes an electron or hole modified by its interactions with the surrounding electronic environment. Its properties, such as energy, are determined by incorporating self-energy corrections through the GW approximation. This method accounts for many-body effects, providing a more accurate description of electronic excitations and band structures compared to standard density functional theory.

$$\Sigma^{\mathrm{GW}}(\mathbf{r},\mathbf{r}',\omega) = \frac{i}{2\pi}\int_{-\infty}^{+\infty} d\omega' e^{i\omega'\eta} G(\mathbf{r},\mathbf{r}',\omega+\omega')W(\mathbf{r},\mathbf{r}',\omega'). \tag{2.2.1}$$

Σ^{GW} in equation 2.2.1 represents the approximation of many-body interactions in the GW formalism, where G is the Green's function describing the propagation of a quasiparticle, and W is the dynamically screened Coulomb interaction. This expression captures the nonlocal and energy-dependent nature of the self-energy.
To better understand Σ^{GW}, we decompose it into its exchange $\Sigma_{\mathrm{x}}^{\mathrm{GW}}$ and correlation Σ_{c}^{GW} contributions. This decomposition is achieved by expressing the screened interaction W as the sum of the bare Coulomb potential V and its screening corrections. Consequently, equation (2.2.2) explicitly separates Σ^{GW} into terms arising from the bare interaction GV and a correction due to the screening $G(W-V)$:

$$\Sigma^{\mathrm{GW}} = GV + G(W-V) = \Sigma_x^{\mathrm{GW}} + \Sigma_c^{\mathrm{GW}}. \tag{2.2.2}$$

Evaluation of Σ^{GW} is a complicated task. Usually, the GW self-energy is computed using noninteracting inputs, typically Kohn-Sham wavefunctions and energies. However, in certain cases, a self-consistent GW approach becomes necessary to achieve more accurate or reliable results.

2.2.1 Evaluation of G.

To evaluate G, we begin by using the non-interacting Green's function G_0, which is derived from the Kohn-Sham energies and wave functions [32].
The expression for the Green's function $G_0(\mathbf{r},\mathbf{r}',\omega)$ in terms of the Kohn-Sham eigenstates $\psi_{n\mathbf{k}}^{\mathrm{KS}}$ and eigenvalues $\epsilon_{n\mathbf{k}}^{\mathrm{KS}}$ is given by:

$$G_0(\mathbf{r},\mathbf{r}',\omega) = \sum_{n\mathbf{k}} \frac{\psi_{n\mathbf{k}}^{\mathrm{KS}}(\mathbf{r})\psi_{n\mathbf{k}}^{*,\mathrm{KS}}(\mathbf{r}')}{\omega - \epsilon_{n\mathbf{k}}^{\mathrm{KS}} \pm \eta}, \tag{2.2.3}$$

which in reciprocal space reads as :

$$G_0(\mathbf{k},\omega) = \frac{1}{\omega - \epsilon_{n\mathbf{k}}^{\mathrm{KS}} + \eta}. \tag{2.2.4}$$

2.2.2 Evaluation of W.

To evaluate

$$W(\mathbf{r},\mathbf{r}',\omega) = \int d\mathbf{r}'' \epsilon^{-1}(\mathbf{r},\mathbf{r}'',\omega) v(\mathbf{r}'',\mathbf{r}') \tag{2.2.5}$$

one computes the inverse dielectric function $\epsilon^{-1}(\mathbf{r},\mathbf{r}'',\omega)$ using the Random Phase Approximation (RPA) [22, 25]. Representing this quantity on the plane-wave basis set, it is necessary to calculate the matrix:

$$\epsilon^{-1}_{\mathbf{G}\mathbf{G}'}(\mathbf{q},\omega) = \delta_{\mathbf{G}\mathbf{G}'} + v(\mathbf{q}+\mathbf{G})\chi_{\mathbf{G}\mathbf{G}'}(\mathbf{q},\omega), \tag{2.2.6}$$

where $\mathbf{G}$ and $\mathbf{G}'$ are reciprocal lattice vectors that index the matrix elements in the reciprocal space representation, the vector $\mathbf{q}$ denotes the wavevector within the first Brillouin zone, representing the momentum transfer and ω corresponds to the frequency of the perturbation, linking to dynamical effects.

The reducible polarizability is given by

$$\chi_{\mathbf{GG'}}(\mathbf{q},\omega) = \sum_{\mathbf{G''}}[\delta_{\mathbf{G_1G_2}} - \chi^0_{\mathbf{G_1G_2}}(\mathbf{q},\omega)v(\mathbf{q}+\mathbf{G_1})]^{-1}_{\mathbf{GG''}}\chi^0_{\mathbf{G''G'}}(\mathbf{q},\omega) \tag{2.2.7}$$

where [33]

$$\chi^0_{\mathbf{GG'}}(\mathbf{q},\omega) = 2\sum_{c,v}\int_{\mathrm{BZ}}\frac{d\mathbf{k}}{(2\pi)^3}\rho^*_{cv\mathbf{k}}(\mathbf{q},\mathbf{G})\rho_{cv\mathbf{k}}(\mathbf{q},\mathbf{G'})f_{v\mathbf{k-q}}(1-f_{c\mathbf{k}})\times$$

$$\left(\frac{1}{\omega+\epsilon^{\mathrm{KS}}_{v\mathbf{k-q}}-\epsilon^{\mathrm{KS}}_{c\mathbf{k}}+i0^+} - \frac{1}{\omega+\epsilon^{\mathrm{KS}}_{c\mathbf{k}}-\epsilon^{\mathrm{KS}}_{v\mathbf{k-q}}-i0^+}\right) \tag{2.2.8}$$

and

$$\rho_{cv\mathbf{k}}(\mathbf{q}+\mathbf{G}) = \int d\mathbf{r}\,\psi^{*\mathrm{KS}}_{c\mathbf{k+q}}(\mathbf{r})e^{-i(\mathbf{q}+\mathbf{G})\cdot\mathbf{r}}\psi^{\mathrm{KS}}_{v\mathbf{k}}(\mathbf{r}). \tag{2.2.9}$$

However, it is important to point out that in many GW calculations, in practice, it is not the ϵ^{-1} of Eq. (2.2.6), together with Eqs. (2.2.7) and (2.2.8), that is used in the calculation of the integral of Eq. (2.2.5) to obtain W.
Usually, the approach used is the Plasmon-Pole Model that we will review briefly here below.

2.2.2.1 Plasmon-Pole Model.

The dependence on ω of the ϵ^{-1} of Eq. (2.2.6) can be modeled as a single pole function as [33]

$$\epsilon^{-1}_{\mathbf{GG'}}(\mathbf{q},\omega) \sim \delta_{\mathbf{GG'}} + \frac{\mathrm{R}_{\mathbf{GG'}}(\mathbf{q})}{(\omega-\Omega_{\mathbf{GG'}}(\mathbf{q})+i0^+)^{-1} - (\omega+\Omega_{\mathbf{GG'}}(\mathbf{q})-i0^+)^{-1}} \tag{2.2.10}$$

where the two plasmon-pole parameters $\mathrm{R}_{\mathbf{GG'}}(\mathbf{q})$ (residual) and $\Omega_{\mathbf{GG'}}(\mathbf{q})$ (energy) are then fitted to match the behavior of ϵ^{-1} (Eqs. (2.2.6), (2.2.7) and (2.2.8)) at $\omega = 0$ and $\omega = i\omega_{\mathrm{p}}$ where ω_{p} is a user-defined imaginary plasmon frequency.
Therefore, we have

$$\Omega_{\mathbf{GG'}} = \omega_p\sqrt{\frac{\epsilon^{-1}_{\mathbf{GG'}}(\mathbf{q},\omega_{\mathrm{p}})\Omega_{\mathbf{GG'}}}{\epsilon^{-1}_{\mathbf{GG'}}(\mathbf{q},0)-\epsilon^{-1}_{\mathbf{GG'}}(\mathbf{q},\omega_{\mathrm{p}})}}, \tag{2.2.11}$$

$$\mathrm{R}_{\mathbf{GG'}} = \frac{\epsilon^{-1}_{\mathbf{GG'}}(\mathbf{q},0)\Omega_{\mathbf{GG'}}}{2}. \tag{2.2.12}$$

The choice of ω_{p} is that it is higher than the plasmon peak in the energy-loss spectrum. This ensures the Plasmon-Pole Model captures the main features of the dielectric function. However, this parameter should be checked as it should not affect the results.

2.2.3 Evaluation of Σ.

Following Eq. 2.2.2 we have

$$\Sigma(\mathbf{r},\mathbf{r'},\omega) = \Sigma^{\mathrm{x}}(\mathbf{r},\mathbf{r'}) + \Sigma^{\mathrm{c}}(\mathbf{r},\mathbf{r'},\omega) \tag{2.2.13}$$

where the expression of Σ^{x} is [33]:

$$\Sigma^{\mathrm{x}}_{n\mathbf{k}} = \langle n\mathbf{k}|\Sigma^{\mathrm{x}}(\mathrm{r},\mathrm{r}')|n\mathbf{k}\rangle = -\sum_{\mathrm{m}}\int_{\mathrm{BZ}}\frac{d\mathbf{q}}{(2\pi)^3}\sum_{\mathbf{G}} v(\mathbf{q}+\mathbf{G})|\rho_{nm}(\mathbf{k},\mathbf{q},\mathbf{G})|^2 f_m(\mathbf{k}-\mathbf{q}). \tag{2.2.14}$$

and the expression of Σ^{c} is [33]:

$$\Sigma^{\mathrm{c}}_{n\mathbf{k}}(\omega) = \langle n\mathbf{k}|\Sigma^{\mathrm{c}}|n\mathbf{k}\rangle = i\sum_{\mathrm{m}}\int_{\mathrm{BZ}}\frac{d\mathbf{q}}{(2\pi)^3}\sum_{\mathbf{G},\mathbf{G}'}\frac{4\pi}{|\mathbf{q}+\mathbf{G}|^2}\rho_{nm}(\mathbf{k},\mathbf{q},\mathbf{G})\rho^*_{nm}(\mathbf{k},\mathbf{q},\mathbf{G}')\times$$

$$\int d\omega' G^0_{m\mathbf{k}-\mathbf{q}}(\omega-\omega')\epsilon^{-1}_{\mathbf{G}\mathbf{G}'}(\mathbf{q},\omega'). \tag{2.2.15}$$

2.2.4 The Quasiparticle Energies.

To obtain the quasiparticle energies, it is considered that the Kohn-Sham (KS) equation describes noninteracting particles moving in an effective potential that includes the external potential, the Hartree term, and the exchange-correlation potential, which is:

$$\left[-\frac{\nabla^2}{2} + V_{\mathrm{ext}}(\mathbf{r}) + \int\frac{\rho^{\mathrm{KS}}(\mathbf{r}')}{|\mathbf{r}-\mathbf{r}'|}d\mathbf{r}' + V_{\mathrm{xc}}[\rho^{\mathrm{KS}}(\mathbf{r})]\right]\psi^{\mathrm{KS}}_i(\mathbf{r}) = \epsilon^{\mathrm{KS}}_i\psi^{\mathrm{KS}}_i(\mathbf{r}), \tag{2.2.16}$$

while the quasiparticle energies are in principle extracted from a similiar equation:

$$\left[-\frac{\nabla^2}{2} + V_{\mathrm{ext}}(\mathbf{r}) + \int\frac{\rho^{\mathrm{GW}}(\mathbf{r}')}{|\mathbf{r}-\mathbf{r}'|}d\mathbf{r}'\right]\psi^{\mathrm{KS}}_i(\mathbf{r}) + \int\Sigma(\mathbf{r},\mathbf{r}',\epsilon^{\mathrm{GW}}_i)\psi^{\mathrm{KS}}_i(\mathbf{r}')d\mathbf{r}' = \epsilon^{\mathrm{GW}}_i\psi^{\mathrm{KS}}_i(\mathbf{r}) \tag{2.2.17}$$

in which the self-energy Σ accounts for dynamic many-body effects and providing a more accurate description of electronic excitations.
By comparing Eqs. 2.2.16 and 2.2.17 it is possible to observe a very similar structure, except that in 2.2.16 the many-body effects are described by the local exchange-correlation potential V_{xc} and, instead in 2.2.17 the many-body effects are described by the non-local self-energy Σ.
Therefore, it is often assumed that in many cases, the KS eigenvalues ϵ^{KS}_i already provide a reasonable estimate of the band structure. Therefore, $\Sigma(\mathbf{r},\mathbf{r}',\epsilon^{\mathrm{GW}}_i) - V_{\mathrm{xc}}(\mathbf{r})\delta(\mathbf{r}-\mathbf{r}')$ is small and justifies the use of first-order perturbation theory to obtain approximate energies:

$$\epsilon^{\mathrm{GW}}_i \approx \epsilon^{\mathrm{KS}}_i + \langle\psi^{\mathrm{KS}}_i|\Sigma(\epsilon^{\mathrm{GW}}_i) - V_{\mathrm{xc}}(\mathbf{r})|\psi^{\mathrm{KS}}_i\rangle. \tag{2.2.18}$$

However, a solution of this nonlinear equation still requires the knowledge of the frequency dependence of the self-energy, which is not known in general.
Therefore, we use the linear expansion:

$$\Sigma(\mathbf{r},\mathbf{r}',\epsilon^{\mathrm{GW}}_i) \approx \Sigma(\mathbf{r},\mathbf{r}',\epsilon^{\mathrm{KS}}_i) + (\epsilon^{\mathrm{GW}}_i - \epsilon^{\mathrm{KS}}_i)\frac{\partial\Sigma(\mathbf{r},\mathbf{r}',\omega)}{\partial\omega}\Big|_{\omega=\epsilon^{\mathrm{KS}}_i} \tag{2.2.19}$$

which leads to:

$$\epsilon^{\mathrm{GW}}_i \approx \epsilon^{\mathrm{KS}}_i + Z_i\left\langle\psi^{\mathrm{KS}}_i\left|\Sigma(\epsilon^{\mathrm{KS}}_i) - V_{\mathrm{xc}}\right|\psi^{\mathrm{KS}}_i\right\rangle \tag{2.2.20}$$

where Z_i is the quasiparticle normalization factor,

$$Z_i = \left(1 - \left\langle\psi^{\mathrm{KS}}_i\left|\frac{\partial\Sigma(\epsilon^{\mathrm{KS}}_i)}{\partial\omega}\right|\psi^{\mathrm{KS}}_i\right\rangle\right)^{-1}. \tag{2.2.21}$$

Equation 2.2.21 relies only on Kohn-Sham inputs, but the derivative of Σ is also needed. In our case, after calculating $\Sigma(\mathbf{r}, \mathbf{r}', \epsilon_i^{\mathrm{KS}}) = \Sigma_{\mathrm{x}}(\mathbf{r}, \mathbf{r}') + \Sigma_c(\mathbf{r}, \mathbf{r}', \epsilon_i^{\mathrm{KS}})$ a numerical method (finite-difference) is used to calculate the derivative. [33]

2.3 G_0W_0 vs Self-Consistent GW.

The quasiparticle energy calculated using Eq. 2.2.20, with ϵ_i^{KS} from methods such as PBE or LDA as the starting point, is referred to as the G_0W_0 approximation.
Here below we write the steps of a G_0W_0 calculation :

1. **Input:** Obtain Kohn-Sham energies and wavefunctions from a DFT calculation.
2. **Calculate G_0:** Compute the non-interacting Green's function using DFT eigenvalues and eigenstates.
3. **Calculate W_0:** Compute the screened interaction from the dielectric function constructed using the DFT eigenvalues.
4. **Compute Σ:** Calculate the self-energy Σ using G_0 and W_0.
5. **Quasiparticle Corrections:** Apply corrections to the Kohn-Sham energies to obtain the quasiparticle energies in the G_0W_0 approximation ϵ_i^{GW}.

In the self-consistent GW method, the goal is to iteratively refine the quasiparticle energies calculated with G_0W_0 by recalculating both the Green's function (G) and the screened Coulomb interaction (W). This ensures that the starting point (e.g., energies and wavefunctions) aligns consistently with the GW approximation, improving accuracy over the one-shot G_0W_0 approach.
Here below we write the steps of a GW calculation :

1. **Initial Step (Starting Point):** The process begins with an initial guess for the Green's function (G_0) and the screened interaction (W_0). These are typically derived from Kohn-Sham energies and wavefunctions obtained using DFT. Then as for the G_0W_0, the quasiparticle energies ϵ_i^{GW} are calculated.
2. **Update the Green's Function (G):** The Green's function is recalculated:

$$G(\mathbf{r}, \mathbf{r}', \omega) = \sum_{n\mathbf{k}} \frac{\psi_{n\mathbf{k}}^{\mathrm{KS}}(\mathbf{r})\psi_{n\mathbf{k}}^{*,\mathrm{KS}}(\mathbf{r}')}{\omega - \epsilon_{n\mathbf{k}}^{\mathrm{GW}} + i\eta}, \tag{2.3.1}$$

3. **Update the Screened Interaction (W):** The screened Coulomb interaction W is updated
4. **Calculate the Self-Energy (Σ):** The self-energy operator Σ is computed using the current Green's function and screened Coulomb interaction.
5. **Recompute Quasiparticle Energies:** With the updated Σ, the quasiparticle energies are recomputed.

6. **Check for Convergence:** The process repeats until the differences in the quasiparticle energy, between successive iterations are below a predefined threshold, indicating self-consistency.

The results are independent of the initial Kohn-Sham starting point, making them more robust. Self-consistent GW provides a more accurate description of the quasiparticle energies, particularly for systems with strong electronic correlations or significant screening effects. Self-consistent GW is more expensive than a single G_0W_0 calculation.

2.4 The Gaps.

To clearly understand the electronic excitations of a system, it is important to have a clear definition of the gaps. In Fig. 2.1 we represent (left) the top valence and bottom conduction bands, and we show the electronic $E_{\text{gap}}^{\text{DFT}}$, i.e. the lowest difference in energy between these two bands. The bands are then corrected by GW, and in the center we show the quasiparticle gap $E_{\text{gap}}^{\text{GW}}$, which usually corrects the understimation of the DFT electronic gap. In this thesis, we shall be calculating these two gaps.
There exists also the optical gap $E_{\text{gap}}^{\text{BSE}}$ which takes into account the electron-hole interaction. It is calculated using the Bethe-Salpeter equation [22] on top of a GW calculation.

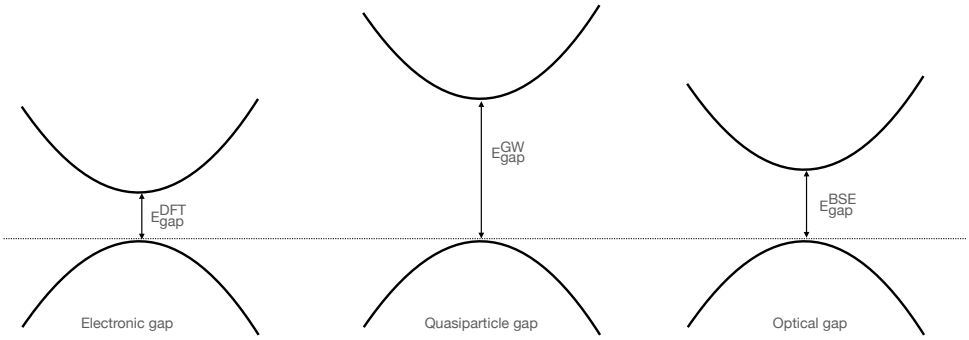

Figure 2.1: The energy gaps : electronic gap $E_{\text{gap}}^{\text{DFT}}$ (left), quasiparticle gap $E_{\text{gap}}^{\text{GW}}$ and optical gap $E_{\text{gap}}^{\text{BSE}}$.

Chapter 3

Computational Details.

In this chapter, we will present the pseudopotentials used and step-by-step convergence processes of all parameters and also report the final converged parameters.

3.1 Choice of Pseudopotentials.

In computational material science, pseudopotentials are essential for simplifying the complex interactions between core and valence electrons, allowing for efficient yet accurate simulations. The choice of pseudopotentials significantly affects the results of electronic structure calculations, making it crucial to select appropriate pseudopotentials that balance accuracy and computational efficiency[34, 35].
The pseudopotentials we tested and that are reported in the tab 3.1 have been generated using the ONCVPSP (Optimized Norm-Conserving Vanderbilt PSeudoPotential) code [36] and were chosen for the study of TiO_2, IrO_2, and SnO_2. They have been tested and their accuracy has been proven in the following studies, together with their compatibility with the computational methods employed to calculate structural, electronic, and optical properties.
In particular, the pseudopotentials that have been finally chosen for the description of the structural, electronic, and optical properties have been bolded.

Table 3.1: Pseudopotentials used for Ti, Ir, Sn, and O, along with their electronic configurations (Elec. Conf.), relativistic effects (Rel. Effects), and the database from which they were downloaded. The only exception are those labelled with an asterics (*) which were generated by my supervisor always using the ONCVPSP code.

Element	Elec. Conf.	Rel. Effects	Database
Ti	$3s^2 3p^6 4s^2 3d^2$	SR	**sg15 (PBE-1.0)** (Tisg15)
	$3s^2 3p^6 4s^2 3d^2$	SR	sg15 (PBE-1.2)
Sn	$4d^{10} 5s^2 5p^2$	SR	sg15 (PBE-1.0)
	$4d^{10} 5s^2 5p^2$	SR	**Dojo (PBE v0.5)** *Standard* (SnDjStn)
	$4s^2 4p^6 4d^{10} 5s^2 5p^2$	SR	**Dojo (PBE v0.5)** *Stringent* (SnDjStr)
	$4s^2 4p^6 4d^{10} 5s^2 5p^2$	SR	**Dojo (PBE v0.5)** *Stringent* (SnDjNoCcStr)*
	$4s^2 4p^6 4d^{10} 5s^2 5p^2$	SR	**Dojo (LDA v0.5)** *Stringent* (SnLDADjStr)*
Ir	$5s^2 5p^6 5d^7 6s^2$	FR	**Dojo (PBE v0.4)** (IrDjFR)
	$5s^2 5p^6 5d^7 6s^2$	SR	**Dojo (PBE v0.5)**(IrDjSR)
O	$2s^2 2p^4$	SR	**sg15_oncv (PBE-1.0)** (Osg15)

3.1.1 Titanium (Ti).

Titanium is a key element in the study of TiO_2. We tested two norm-conserving pseudopotentials that can accurately represent the $3s^2 3p^6 4s^2 3d^2$ electronic configuration. This configuration is crucial for capturing the correct electronic structure of titanium in the compound. Scalar relativistic (SR) effects were included in the pseudopotential to account for relativistic corrections, which are significant but not overwhelming for elements like titanium. This balance ensures that the calculations remain computationally feasible while maintaining high accuracy. The pseudopotentials were downloaded from the sg15 library and correspond to PBE versions 1.0 (Tisg15) and 1.2.

3.1.2 Iridium (Ir).

For iridium, which plays a crucial role in IrO_2, two norm-conserving pseudopotentials from the Dojo library were employed. These pseudopotentials were selected for their accuracy in representing the $5s^2 5p^6 5d^7 6s^2$ configuration of iridium while maintaining computational efficiency. Given iridium's high atomic number, one pseudopotential includes scalar relativistic effects (IrDjSR), while another incorporates fully relativistic effects (IrDjFR). Fully relativistic effects were incorporated into the pseudopotential to account for relativistic energy shifts, which are essential for accurate electronic structure calculations. The inclusion of fully relativistic effects ensures that the significant spin-orbit coupling in iridium is accurately modeled, thereby improving the reliability of the results. We decided to use norm-conserving pseudopotential with SR and with FR because for material such as Ir, the relativistic corrections can significantly impact the optical properties that we plan to calculate in the GW-BSE framework.
For GW-BSE calculations on heavy materials like iridium, using FR pseudopotentials is generally preferable to obtain an accurate description of electronic and optical properties because these pseudopotentials fully account for relativistic effects, including spin-orbit coupling. Using SR pseudopotentials might neglect these effects, leading to less accurate results, especially for optical properties.

3.1.3 Tin (Sn).

Initially, tin (Sn) in SnO_2 was modeled using the sg15 PBE_1.0 with SR approach and an electronic configuration of $4d^{10} 5s^2 5p^2$. This pseudopotential was chosen because norm conserving potentials are effective for elements with semi-core states, allowing for a flexible representation of the valence wavefunctions. The scalar relativistic effects were included to account for relativistic corrections, which are significant for tin due to its atomic number.
However, the band structure calculations revealed unexpected flat bands, which indicated that the pseudopotential might not have accurately captured the electronic properties of tin. This unexpected result suggested to discard this pseudopotential and to use another one, maybe with also a more accurate electronic structure calculations for SnO_2.
We downloaded the NC PBE_0.5 with SR corrections from the Dojo database. Specifically, one pseudopotential has the electronic configuration $4d^{10} 5s^2 5p^2$, which we labeled as *Standard* (SnDjSta), while another has the electronic configuration $4s^2 4p^6 4d^{10} 5s^2 5p^2$, which we labeled as *Stringent* (SnDjStr). We considered two pseudopotentials with different electronic configurations to investigate whether it is important to complete the inner shell for an accurate description of the optical properties of SnO_2.

Furthemore, in the developing of our research we realised that the Dojo pseudopotentials have been all generated by applying a core correction. Core correction improve the accuracy in the DFT calculations, but they are not implemented in the Yambo code for the GW and So this leads to a mismatch. When computing the quasiparticle correction, we perform $\Sigma - V_{\text{xc}}$ (see Chapter 2 Eq. 2.2.18).
Therefore, my supervisor generated with the ONCVPSP code, a pseudopotential with exactly the same parameters used to generate SnDjStr except for the inclusion of the core corrections. This will permit us to estimate the errors we make on the quasiparticle energies.
Moreover, always because of our progression on the investigation into the properties of SnO_2, compelled my supervisor to generate another additional pseudopotential, still based on the characteristics of the SnDjStr but with LDA exchange-correlation functional instead of PBE.

3.1.4 Oxygen (O).

Oxygen is a common element in the three compounds (TiO_2, IrO_2, and SnO_2) and was modeled using a PBE norm-conserving pseudopotential from the sg15 library (Osg15). This pseudopotential accurately represents the $2s^2 2p^4$ electronic configuration of oxygen. Although oxygen is a light element, scalar relativistic effects were included to account for any minor relativistic corrections that could impact the accuracy of the electronic structure calculations. The inclusion of these effects ensures a more precise representation of the oxygen's behavior in the compounds studied.

3.1.5 Justification of Pseudopotential Choices.

The pseudopotentials chosen for titanium, tin, iridium, and oxygen were selected to strike a balance between accuracy and computational efficiency, ensuring reliable results while minimizing computational costs. Scalar relativistic corrections were used for titanium, iridium, tin and oxygen to capture essential relativistic effects without the need for fully relativistic pseudopotentials, which would be more computationally demanding. For Ir, fully relativistic effects were also included due to the significant spin-orbit coupling present, ensuring accurate modeling of its electronic structure.
This careful selection of pseudopotentials ensures that the electronic structure and related properties of TiO_2, IrO_2, and SnO_2 are represented accurately in the simulations.

3.2 Convergence of DFT Calculations.

3.2.1 Cutoff Energy Convergence.

In this section, we present the cutoff energy (E_{cut}) convergence analysis for the three materials: TiO_2, IrO_2 and SnO_2. The cutoff energy was varied, and the corresponding total energies were noted until they converged. The convergence criterion was based on the difference in total energy between consecutive E_{cut} values until a desired precision limit of below 1 meV was achieved.

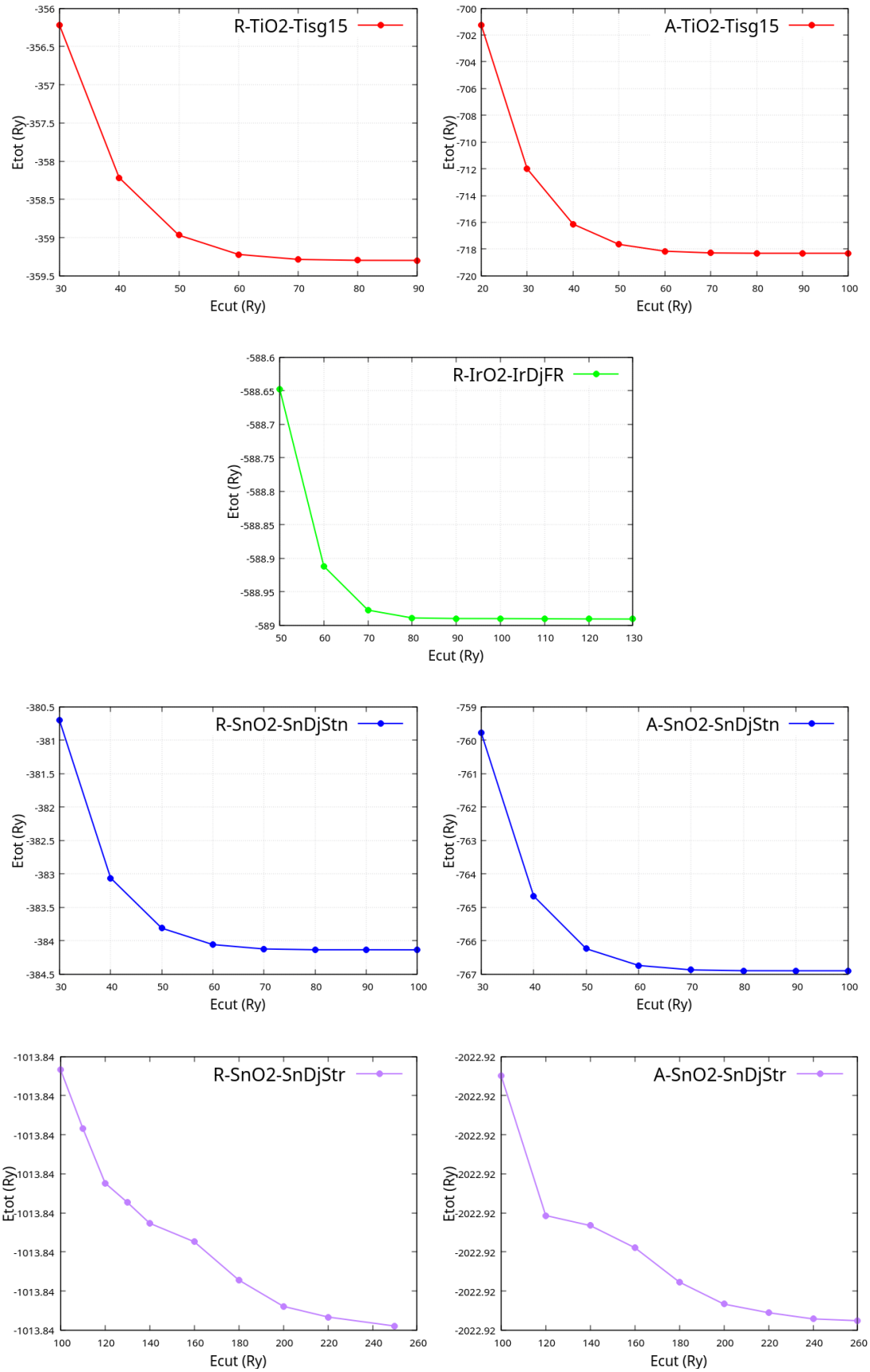

Figure 3.1: E_{cut} convergence plots for rutile TiO_2, anatase TiO_2 , rutile IrO_2, rutile SnO_2 and anatase SnO_2 respectively. For each compound, a 224 k-points grid was used to sample the Brillouin zone except for anatase phases where 422 k-points grid was used. The pseudopotentials used are: Tisg15, SnDjStn, IrDjFR and Osg15.

In Figure 3.1, we present the convergence plots for TiO_2 (using the Tisg15 pseudopotential for Ti), IrO_2 (using the IrDjFR pseudopotential for Ir), and SnO_2 (using the SnDjStn and SnDjStr pseudopotentials for Sn). For all oxides, the Osg15 pseudopotential was used for oxygen. Each compound was sampled over a 224 k-point grid in the Brillouin zone except for anatase phases where 422 k-points grid was used.
The convergence plots show that the total energy stabilizes as E_{cut} increases, indicating that the selected cutoff energy is sufficient to capture the system's electronic properties accurately. The estimated differences in the total energies with the final chosen cutoff energy are within the desired precision limits of below 1 meV, leading to a high degree of accuracy in our results. The values of E_{cut} used in the calculations are reported in tab3.2, together with the pseudopotentials used. For IrO_2, when using the IrDjSR pseudopotential for Ir, we will apply the same E_{cut} as used with the IrDjFR pseudopotential.

Table 3.2: Final cutoff energy values for different phases of TiO_2, IrO_2, and SnO_2. The values were determined based on convergence tests using a 224 k-points grid.

Compound	Phase	Final Cutoff Energy (Ry)	Pseudopotentials
TiO_2	Rutile	60 Ry	Tisg15/Osg15
TiO_2	Anatase	80 Ry	Tisg15/Osg15
IrO_2	Rutile	70 Ry	IrDjFR/Osg15
SnO_2	Rutile	80 Ry	SnDjSta/Osg15
SnO_2	Rutile	220 Ry	SnDjStr/Osg15
SnO_2	Anatase	80 Ry	SnDjSta/Osg15
SnO_2	Anatase	220 Ry	SnDjStr/Osg15

3.2.2 K-points Convergence.

This section presents the k-points convergence analysis for TiO_2, IrO_2, and SnO_2 using the same pseudopotentials used for E_{cut} convergence of Figure 3.1.
For each system, the number of k-points was varied, and the total energies were calculated to ensure convergence. The final k-points grid was chosen based on the stability of the total energy as the number of k-points increased.
The convergence was performed using the fixed cutoff energy values reported in tab3.2. The convergence plots in Figure 3.2 show how the total energy stabilizes as the number of k-points increases. This stabilization indicates that the selected k-points grid is dense enough to ensure accurate electronic structure calculations. The differences in total energies between the selected k-points and denser grids were within acceptable precision limits, ensuring reliable calculations.

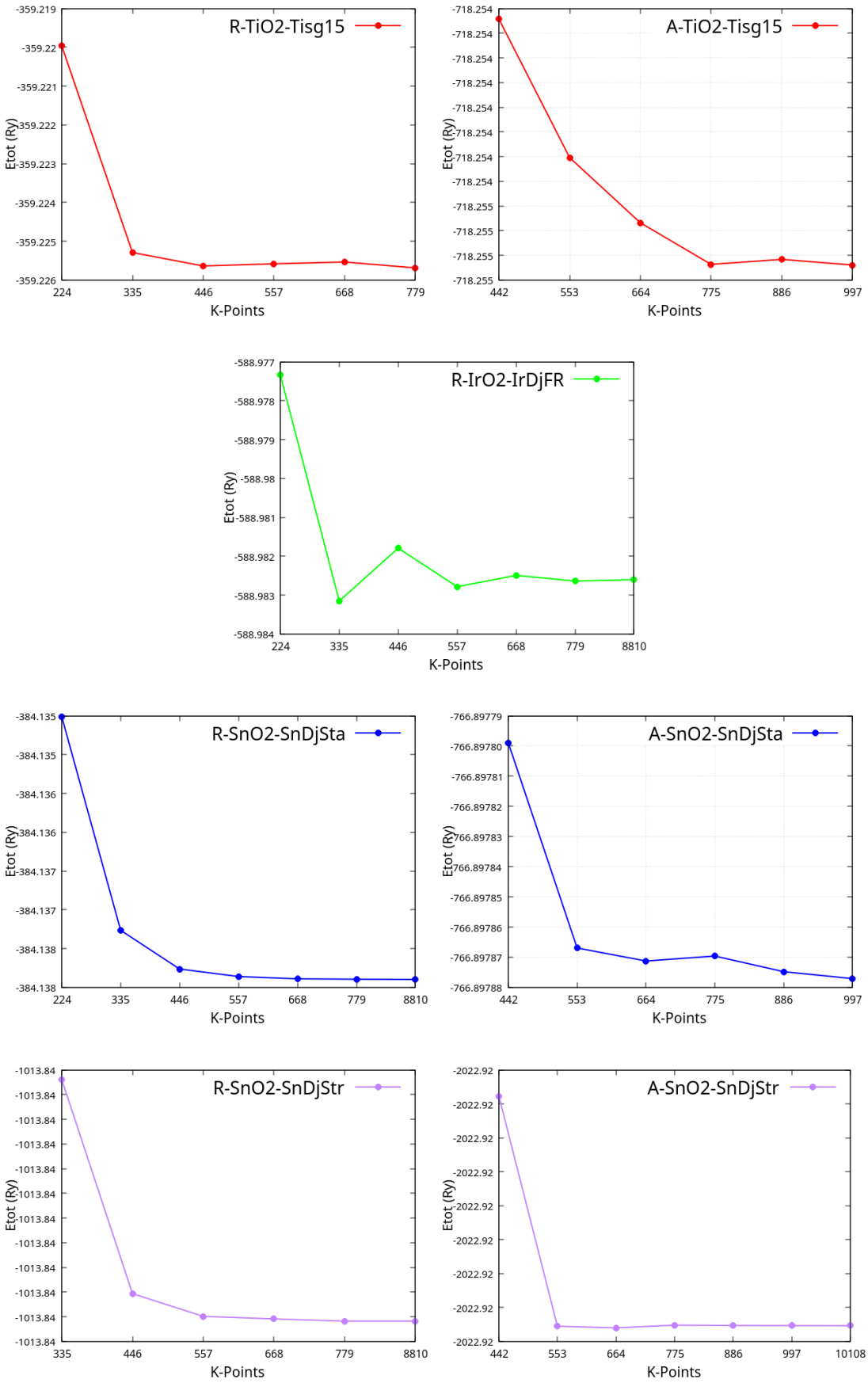

Figure 3.2: K-points convergence analysis for for rutile TiO_2 (a), anatase TiO_2 (b), rutile IrO_2 (c), rutile SnO_2 (d) and anatase SnO_2 (e) using the respective converged E_{cut} in 3.2. The pseudopotentials used are: Tisg15, SnDjStn, IrDjFR and Osg15.

The final values of k-points used in the calculations are reported in tab3.3 together with the pseudopotentials used. Also in this case, for IrO, when using the IrDjSR pseudopotential for Ir, we will apply the same k-point grid as used with the IrDjFR pseudopotential.

Table 3.3: Final k-points grid for different phases of TiO_2, IrO_2, and SnO_2. The values were determined based on convergence tests using a fixed E_{cut} specified in Table3.2.

Compound	Phase	Final k-points Grid	Pseudopotentials
TiO_2	Rutile	$7 \times 7 \times 9$	Tisg15/Osg15
TiO_2	Anatase	$9 \times 9 \times 7$	Tisg15/Osg15
IrO_2	Rutile	$6 \times 6 \times 8$	IrDjFR/Osg15
SnO_2	Rutile	$5 \times 5 \times 7$	SnDjSta/Osg15
SnO_2	Rutile	$7 \times 7 \times 9$	SnDjStr/Osg15
SnO_2	Anatase	$9 \times 9 \times 7$	SnDjSta/Osg15
SnO_2	Anatase	$8 \times 8 \times 6$	SnDjStr/Osg15

3.3 Convergence of GW calculations for SnO_2.

3.3.1 Convergence of Parameters

GW calculations were performed for both rutile and anatase SnO_2 using both SnDjStn and SnDjStr pseudopotentials. Before performing GW calculations, both self-consistent and non-self-consistent calculations were performed, adjusting the number of k-points and bands according to the convergence results of the GW.
The GW convergence is achieved when $\Delta E_{\text{gap}} = E_{\text{gap}}^{\text{GW}} - E_{\text{gap}}^{\text{DFT}}$ is less than 1 meV.
For accurate GW calculations, the convergence of some parameters was crucial. The convergence was done on a total of 5 parameters: **BndsRnXp**, **NGsBlkXp**, **GbndRnge**, **EXXRLvcs** and **VXCRLvcs**. Below is the interpretation of each parameter and how it relates to the GW predictions of the band gap:

- BndsRnXp: Defines the range of electronic bands (both empty and filled) used in constructing the screened interaction W within the GW approximation. Specifically, this parameter limits the set of bands included in the calculation of the ϵ^{-1} (equation 2.2.6), which directly impacts the accuracy and computational cost of the GW self-energy calculation.

- NGsBlkXp: This specifies the size of the dielectric matrix ϵ^{-1} (equation 2.2.6)in terms of the number of G-vectors (plane waves) used to represent the screened Coulomb interaction W in the GW approximation. Essentially, it controls the number of plane waves considered in the screening calculation. The dielectric function is constructed as a matrix, and NGsBlkXp determines the cutoff for G-vectors in this matrix, influencing the accuracy of the screening process. Also, it specifies the number of G-vectors in Σ^c (equation 2.2.15)

- GbndRnge: This specifies the range of electronic bands (occupied and unoccupied) used in calculating Σ^c (equation 2.2.15)

- EXXRLvcs: Specifies the cutoff for the number of reciprocal lattice vectors (G-vectors) included in the calculation of the exact exchange (EXX) component of

screened Coulomb interactions. This parameter determines the plane-wave cutoff energy for the G-vectors used to build the exchange operator Σ^x (equation 2.2.14).

- VXCRLvcs: is a parameter that controls the plane-wave cutoff for the G-vectors used in the calculation of the exchange-correlation potential V_{xc}.

To achieve convergence, we followed a specific procedure. First, we fixed EXXRLvcs and VXCRLvcs at 10000 Ry and then converged BndsRnXp, NGsBlkXp, and GbndRnge. After this, we increased EXXRLvcs and VXCRLvcs, keeping the other three parameters fixed at their respective converged values until full convergence.
After converging all the parameters above, it was worthwhile to check over the k-points. For this step it was necessary to start from the code Quantum Espresso and redo the self-consistent and non-self-consistent calculations for larger k-points grids. It can be easily seen that the grid 557 is enough to fully converge.
The results of this procedure are shown for rutile SnO_2 with the SnDjSta pseudopotential in Table 3.4, Table 3.5 and Table 3.6. Moreover, the above procedure was then repeated for rutile SnO_2 with DjSnStr pseudopotential and for anatase SnO_2 with DjSnSta and DjSnStr pseudopotential. All results are in Appendix **??**.

Table 3.4: Rutile SnO_2 convergence results of BndsRnXp, NGsBlkXp and GbndRnge using SnDjSta.

BndsRnXp	**NGsBlkXp (Ry)**	**GbndRnge**	Δ**E$_{gap}$(eV)**
100	5	100	0.748164
100	7	100	0.823922
100	9	100	0.850917
100	12	100	0.874582
100	15	100	0.887867
100	18	100	0.893494
100	21	100	0.896071
100	24	100	0.897637
300	9	300	0.808824
500	9	500	0.823545
800	9	800	0.829289
1100	9	1100	0.831138
1300	9	1300	0.831926

In Table 3.4, it can be seen that keeping BndsRnXp and GbndRnge constant and increasing NGsBlkXp, stablised the ΔE_{gap} at 0.887867 eV when NGsBlkXp is 15 Ry.
NGsBlkXp was then kept constant but this time at lower value to reduce the computational cost, BndsRnXp and GbndRnge were increased until again the ΔE_{gap} at 0.831138 eV. This marked the end of the convergence of the first three parameters.
These converged parameters were then adopted to converge EXXRLvcs and VXCRLvcs which converged at 10000 RL (Reciprocal Lattice units) Table 3.5.
Table 3.6 shows that the k-points grid 557 is sufficient to converge, and the final converged parameters are reported in Table 3.7. These converged parameters were adopted for GW calculations reported and discussed in Chapter 5.

However,in the case of anatase structure,owing to a lack of time, we were unable to complete the final calculation with all converged parameters for GW in the case of both SnDjSta and SnDjStr pseudopotentials. In Chapter 5 the calculation we report for GW with SnDjSta was performed with 553 k points, BndsRnXp = 800, NGsBlkXp = 21 Ry, GbndRnge = 800 and EXXRLvcs = VXCRLvcs = 10000 RL.

Table 3.5: Rutile SnO_2 convergence results of EXXRLvcs and VXCRLvcs using SnDjSta pseudopotential. We used for these calculations: BndsRnXp=1100, NGsBlkXp=15 Ry and GbndRnge=1100.

EXXRLvcs/VXCRLvcs (RL)	ΔE_{gap}**(eV)**
8000	0.957464
10000	0.956478
12000	0.954322

Table 3.6: Rutile SnO_2 convergence results of k-Points using using SnDjSta pseudopotential. We used for these calculations: BndsRnXp=500, NGsBlkXp=9 Ry and GbndRnge=500.

K-Points	ΔE_{gap}**(eV)**
779	0.829721
557	0.823545

Table 3.7: Converged parameters used in GW calculations for both phases of SnO_2 and both SnDjSta and SnDjStr pseudopotentials .

Phase	**PP**	**BndsRnXp**	**NGsBlkXp (Ry)**	**GbndRnge**	**K-Points**	**EXXRLvcs/VXCRLvcs (RL)**
Rutile	SnDjSta	1100	15	1100	5 5 7	10000
	SnDjStr	800	21	800	668	10000
Anatase	SnDjSta	1100	21	1100	664	10000
	SnDjStr	800	21	800	664	10000

Chapter 4

Results and Discussion on TiO_2 and IrO_2 .

In this Chapter, we focus on TiO_2 in both the rutile and anatase phases, which was the first material we studied. It served as a starting point for establishing a framework to investigate the structural properties and electronic excitations of oxides. The extensive literature available on this material provided a significant advantage, enabling us to validate and compare our findings effectively.
We also began studying the structural properties and electronics excitations of IrO_2. However, the metallic nature of this material introduces additional complexity in the calculation of its optical properties. Recently, León *et al.* [37] proposed a new methodology that offers an effective strategy for performing GW calculations beyond the Plasmon-Pole approximation, while being less computationally expensive than full-frequency approaches. However, due to the complexity of the problem, we determined that a longer timeframe would be required to properly implement and develop this method.
As a result, we focused solely on the structural properties of IrO_2, specifically analyzing the role of scalar and relativistic corrections in pseudopotentials. This serves as a foundation for future investigations into the electronic excitations of this material.

4.1 Structural Properties.

4.1.1 TiO_2.

Titanium is a transition metal present in the 4^{th} column of the periodic table having atomic numbers 22, while oxygen is a gas found in the 16th column of the periodic table[38]. The rutile structure of TiO_2 is tetragonal with space group $P4_2/mnm$ (No 136) and optimized lattice parameters of approximately $a = b = 4.55$ Å and
$c = 2.93$ Å, comparable with previous reports[39]. In this structure, each Ti atom is coordinated by six O atoms in an octahedral configuration. These TiO_6 octahedra share edges along the c axis and corners in the ab plane, forming a dense and compact arrangement[40].
The atomic positions in the unit cell are as follows:

- Ti atoms: $(0, 0, 0)$ and $(\frac{1}{2}, \frac{1}{2}, \frac{1}{2})$
- O atoms: $(u, u, 0)$ and $(\frac{1}{2} + u, \frac{1}{2} - u, \frac{1}{2})$, where $u \approx 0.305$

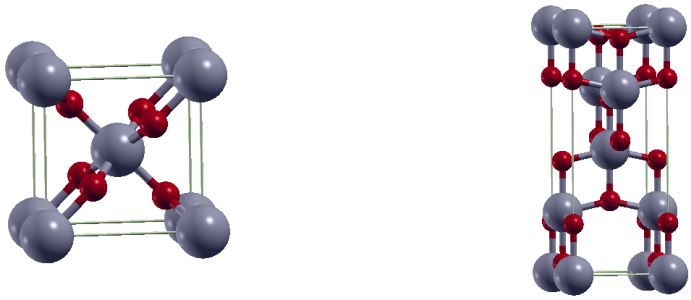

(a) (b)

Figure 4.1: optimized rutile and anatase structures of the primitive unit cell of TiO_2.

The anatase structure of TiO_2 is also tetragonal, but with a different space group, $I4_1/amd$ (No 141), and the optimized lattice parameters $a = b = 3.80$ Å and $c = 9.67$ Å comparable with the previous reports[39] . Similar to rutile, each Ti atom is surrounded by sivcrelax.outx O atoms in an octahedral geometry. However, in anatase, the TiO_6 octahedra are arranged differently, sharing only corners, resulting in a more open structure compared to rutile.
The atomic positions in the unit cell are as follows:

- Ti atoms: $(0, 0, 0)$ and $(\frac{1}{2}, \frac{1}{2}, \frac{1}{4})$
- O atoms: $(0, 0, u)$ and $(0, \frac{1}{2}, \frac{1}{4} + u)$, where $u \approx 0.208$

The optimized rutile and anatase structures of the primitive unit cell of TiO_2 are shown in Figure 4.1.
In Table 4.1 we reported the optimized values of the lattice parameters and bond lengths. We note that Ti forms an octahedron with the surrounding 6 oxygen, therefore we report two Ti-O bond length, which corresponds to axial and planar direction of the octahedron. In particular, Ti-O distances are larger along the axial direction than in the planar direction of the octahedron.

Table 4.1: Lattice parameters and bond lengths for TiO2 in rutile and anatase phases.

Material	Phase	Refs.	a(Å)	c(Å)	Bond Lengths (Å)
TiO_2	Rutile	This work	4.55	2.93	Ti-O: 1.94, 1.95
TiO_2	Rutile	[41]	4.59	2.95	Ti-O: 1.95, 1.98
TiO_2	Rutile	Exp. [12]	4.59	2.95	Ti-O: 1.95,1.98
TiO_2	Rutile	Exp. [14]	4.59	2.96	Ti-O: 1.95,1.98
TiO_2	Anatase	This work	3.80	9.67	Ti-O: 1.95,2.00
TiO_2	Anatase	[41]	3.78	9.50	Ti-O: 1.93, 1.98
TiO_2	Anatase	Exp.[12, 14]	3.78	9.50	Ti-O: 1.94, 1.97

4.1.2 IrO_2.

Likewise, iridium is a transition metal present in the 9^{th} column of the periodic table having atomic numbers 77 [38].The rutile structure of IrO_2 is tetragonal with space group $P4_2/mnm$ (No 136) and the optimized lattice parameters of approximately $a = b = 4.531$ Å and $c = 3.147$ Å. In this structure, each Ir atom is coordinated by six O atoms in an octahedral configuration. These IrO_6 octahedra share edges along the c axis and corners in the ab plane, forming a dense and compact arrangement[40].
The atomic positions in the unit cell are as follows:

- Ir atoms: $(0, 0, 0)$ and $(\frac{1}{2}, \frac{1}{2}, \frac{1}{2})$
- O atoms: $(u, u, 0)$ and $(\frac{1}{2} + u, \frac{1}{2} - u, \frac{1}{2})$, where $u \approx 0.305$

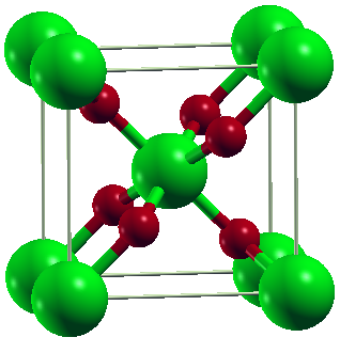

Figure 4.2: optimized rutile structure of the primitive unit cell of IrO_2.

The optimized rutile structure of the primitive unit cell of IrO_2 is shown in Figure 4.2. In Table4.2 we report the optimized values of the lattice parameters and bond lengths. We note that Ir forms an octahedron with the six surrounding oxygen atoms. Therefore, we report two Ir-O bond lengths, which correspond to the axial and planar directions of the octahedron. In particular, Ir-O distances are larger along the axial direction than in the planar direction of the octahedron.

Table 4.2: Lattice parameters and bond lengths for IrO_2 in rutile and anatase phases Tisg15.

Material	Phase	Refs.	a(Å)	c(Å)	Bond Lengths (Å)
IrO_2 (DjIrFR)	Rutile	This work	4.54	3.17	Ir-O:1.98, 2.01
IrO_2 (DjIrSR)	Rutile	This work	4.53	3.17	Ir-O:1.97, 2.01
IrO_2	Rutile	[42]	4.54	3.16	Ir-O:1.97, 1.76
IrO_2	Rutile	Exp.[43]	4.51	3.16	

4.2 Electronic Properties.

4.2.1 TiO_2.

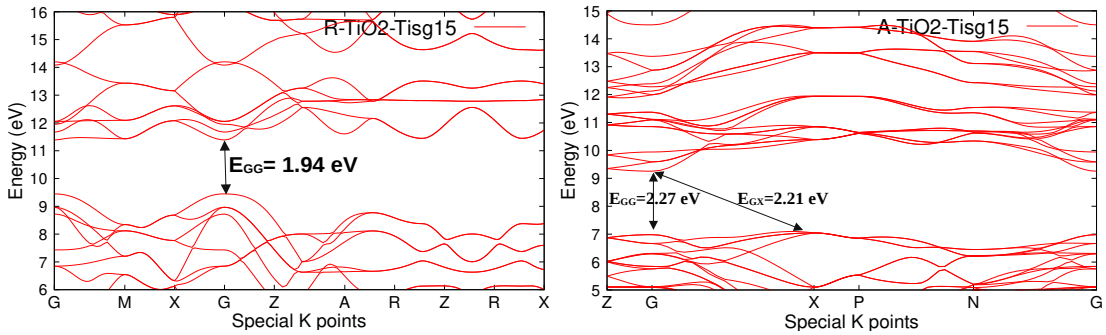

(a) (b)

Figure 4.3: Electronic band structure of rutile TiO_2 (a) and anatase TiO_2 (b) along the high symmetry directions computed using the selected parameters in Table 3.2 and 3.3.

In Figure 4.3, we present the electronic band structure of TiO_2 calculated at the DFT/PBE level along the high-symmetry directions. The computed band gaps for rutile and anatase TiO_2 are 1.94 eV (direct gap) and 2.21/2.27 eV (indirect/direct gap), respectively, in good agreement with the previous findings of Chiodo *et al.* [41] (see Table 4.3).
However, the electronic gaps for the two phases are underestimated by 1.06 eV for rutile and 0.93-0.99 eV for anatase with respect to the experimental data available [10, 12, 13, 14]. Such a behavior is not surprising, as DFT with standard local or semi-local exchange–correlation functionals usually underestimates significantly the band gap [22, 23]. These discrepancies are caused by the lack of the discontinuity of the exchange-correlation potential in going from the valence to the conduction band [44]. To overcome this an efficient strategy is to use the GW approximation, which considers the energies of the quasiparticles [24].
In Chiodo *et al.* [41], calculations of the optical properties using GW-BSE were also performed. For reasons of time, we did not continue with TiO_2, as we preferred to focus on SnO_2, which is a less-studied material with more aspects yet to be understood.

Table 4.3: DFT/PBE band gaps for rutile and anatase TiO_2. The rutile direct gap at Γ is reported and for anatase indirect band gap at X-Γ and direct band gap at Γ are also reported.

Material	Phase	Refs.	E_{Gap}^{DFT}
TiO2	Rutile	This work	1.94
TiO2	Rutile	[41]	1.93
TiO2	Rutile	Exp. [10, 12, 13, 14]	3.0
TiO2	Anatase	This work	2.21/2.27
TiO2	Anatase	[41]	2.15/2.43
TiO2	Anatase	Exp. [12, 13, 14]	3.2

4.2.2 IrO_2.

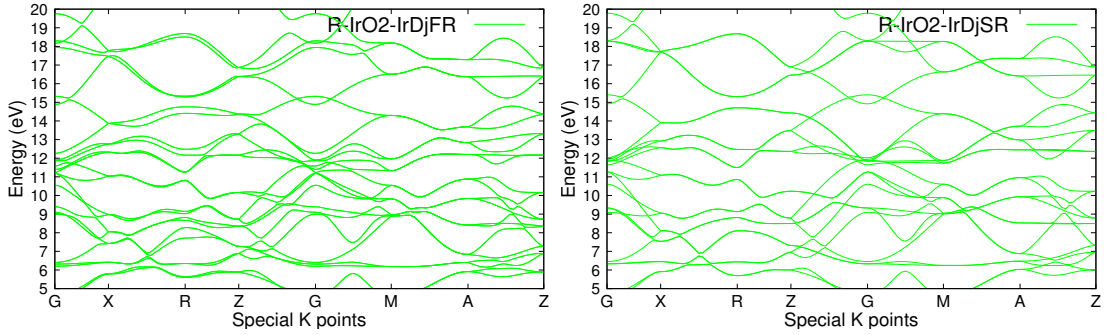

(a) (b)

Figure 4.4: Electronic band structure of rutile IrO_2 using two pseudopotentials along the high symmetry directions computed using the selected parameters in Table 3.2 and 3.3.

In Figure 4.4, we present the electronic band structure of IrO_2 calculated at the DFT/PBE level along the high-symmetry directions. DFT calculations show that IrO_2 is a conductor, with an overlap between the valence band and the conduction band, typical of a metallic material.
From the comparison of the two band structures calculated with the IrDjFR and IrDjSR pseudopotentials, we can observe some differences, which we expect will also affect the GW calculations. This clearly shows the importance of relativistic corrections for IrO_2.
When we started investigating how to proceed for GW corrections we became aware of these two important works [37, 45]. Here, it is pointed out that the properties of metallic systems are challenging to describe with simple models like the plasmon pole approximation (PPA), and more accurate and sometimes prohibitive full-frequency approaches are usually required. In Refs. [37, 45] a new numerical approach is proposed that takes into account the frequency dependence of screening through the multipole approximation (MPA), an accurate and efficient alternative to current full-frequency methods that was recently developed and validated for semiconductors and overcomes several limitations of PPA.
In this case as well, we decided to stop at this point, as performing GW calculations for a metal is a challenging task that requires more time and study than we currently have.

We believe that addressing questions regarding the role of relativistic corrections in the GW band structure of metallic IrO_2 deserves a dedicated, independent study.

Chapter 5

Results and Discussion on SnO_2.

In this chapter, we discuss the electronic properties of SnO_2. We describe its structure and examine how it depends on the choice of pseudopotentials. Additionally, we investigate the quasiparticle gap calculated in GW.
In the following discussion, it is important to note that the widely accepted value of 3.6 eV is considered the band gap of SnO_2. However, this value refers to the optical gap which would be correctly calculated in GW-BSE. What we calculate is the quasiparticle gap in GW, without BSE. The difference between GW and BSE has been estimated to be 30 meV. Therefore, in the following, we will anyway compare the quasiparticle GW gap with the experimental optical gap of 3.6 eV. [46]

5.1 Structural Properties.

Tin (Sn) is a 14^{th} group metal with atomic number 50 which is also found in the form of various oxides in nature. The rutile structure of SnO_2 is tetragonal with space group $P4_2/mnm$ (No. 136), and the optimized lattice parameters of approximately $a = b = 4.82$ Å and $c = 3.25$ Å, comparable to previous studies[40] and the little variation could be due to pressure effects in the previous study. Similarly to TiO_2, each Tin(Sn) atom is coordinated by six oxygen (O) atoms in an octahedral configuration. These SnO_6 octahedra share edges along the c axis and corners in the abplane, forming a dense and compact arrangement.
The atomic positions in the unit cell are as follows:

- Sn atoms: $(0, 0, 0)$ and $(\frac{1}{2}, \frac{1}{2}, \frac{1}{2})$
- O atoms: $(u, u, 0)$ and $(\frac{1}{2} + u, \frac{1}{2} - u, \frac{1}{2})$, where $u \approx 0.305$

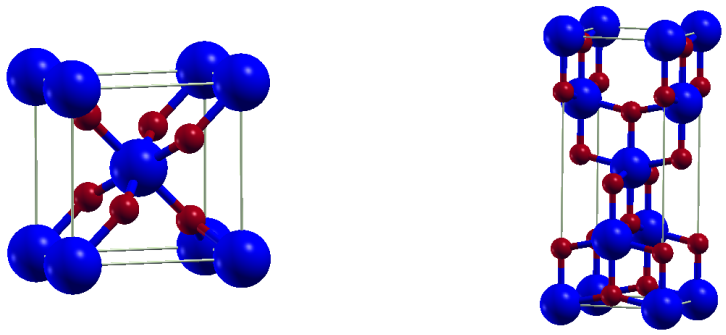

(a) (b)

Figure 5.1: Shows the optmized rutile and anatase structures of the primitive unit cell of SnO_2.

Likewise, the anatase structure of SnO_2 is tetragonal, but with a different space group, $I4_1/amd$ (No. 141), and the optimized lattice parameters $a = b = 3.66$ Å and $c = 8.12$ Å. Similarly to rutile, each Sn atom is surrounded by six O atoms in an octahedral geometry. However, in anatase, the SnO_6 octahedra are arranged differently, sharing only the corners, which results in a more open structure compared to rutile.
The atomic positions in the unit cell are the following:

- Sn atoms: $(0, 0, 0)$ and $(\frac{1}{2}, \frac{1}{2}, \frac{1}{4})$
- O atoms: $(0, 0, u)$ and $(0, \frac{1}{2}, \frac{1}{4} + u)$, where $u \approx 0.208$

The optimized rutile and anatase structures of the primitive unit cell of SnO_2 are shown in Figure5.1.
In Table5.1 we reported the optimized values of the lattice parameters and bond lengths. We note that Sn forms an octahedron with the surrounding 6 oxygen. Therefore, we report two Sn-O bond lengths, which correspond to the axial and planar direction of the octahedron. In particular, Sn-O distances are larger along the axial direction than in the planar direction of the octahedron. It is important to observe that DFT/LDA give results closer to experiments than DFT/PBE.

Table 5.1: Lattice parameters and bond lengths for TiO2, SnO2, and IrO2 in rutile and anatase phases.

Material	Phase	Refs	a(Å)	c(Å)	Bond Lengths (Å)
SnO2	Rutile	This work (SnDjSta)	4.82	3.25	Sn-O: 2.09,2.09
SnO2	Rutile	This work (SnDjStr)	4.82	3.24	Sn-O: 2.09,2.09
SnO2	Rutile	This work (SnDjNoCcStr)	4.83	3.24	Sn-O: 2.09,2.09
SnO2	Rutile	This work (SnDjLDAStr)	4.73	3.19	Sn-O: 2.05,2.06
SnO2	Rutile	[47]	4.74	3.19	
SnO2	Rutile	[40]	4.72	3.19	
SnO2	Rutile	Exp.[43, 48]	4.74	3.19	
SnO2	Anatase	This work (SnDjSta)	3.66	8.12	Sn-O: 2.04,2.06

5.2 Electronic Properties (DFT and GW).

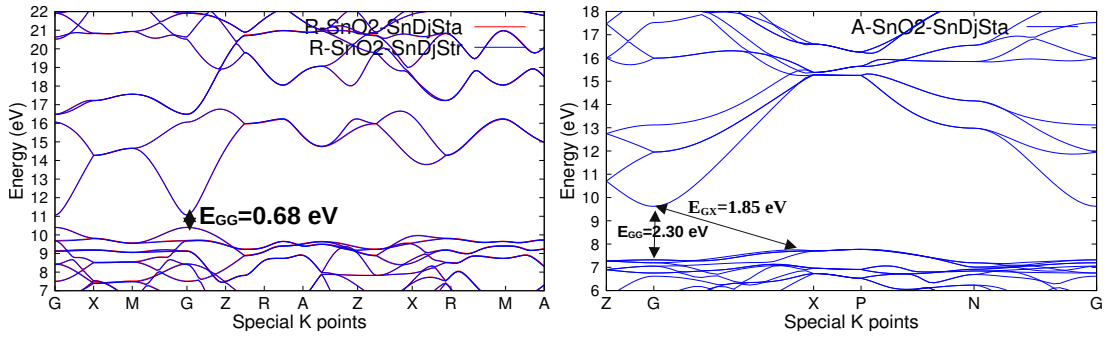

(a) (b)

Figure 5.2: Electronic band structure of rutile SnO_2 (a) and anatase SnO_2 (b) along the high symmetry directions computed using the selected parameters in Table3.2 and 3.3.

In Figure 5.2 we present the electronic band structure of SnO_2 calculated at the DFT/PBE level along the high-symmetry directions and using SnDjSta and DjSnStr pseudopotentials. For rutile SnO_2 there is no significant difference between the two pseudopotentials, which implies that there is no effect of including the 4s and 4p in the valence at the DFT/PBE level. For anatase SnO_2, we did calculations only with SnDjSta at the DFT/PBE level and we obtained an indirect gap at Γ and the indirect gap along Γ-X .

In Fig. 5.3 we also compared the DFT bands calculated with the SnDjStr pseudopotential with the pseudopotential SnDjNoCcStr which do not include core corrections. Also in this case we do not observe variations. Instead, when using the SnLDAStr pseudopotential, we employ LDA instead of PBE, resulting in a rigid shift of ~ 0.5 eV in the bands.

In Table 5.2, we report the direct gap at Γ that we calculated for rutile SnO_2, confirming that LDA gives larger gap than PBE and therefore seems to be closer to experiment. This behaviour is due to the fact that LDA more accurately describes local chemical interactions and the crystalline structure of SnO_2. This can be observed when compared to the experimental values (see Tab. 5.1).

For rutile phase, comparing our DFT/PBE and DFT/LDA results with similar calculations in literature we have found a good agreement. The very high value of the LDA gap from Ref. [49] is due to the fact that scalar relativisitc corrections have not been included in the pseudopotential. The electronic gaps are strongly underestimated with respect to the experimental data available.

In the G_0W_0 framework, starting with the SnDjNoCcStr pseudopotential, the calculated band gap was significantly underestimated by 1.55 eV compared to the experimental value of 3.56 eV. This demonstrates the inherent limitations of this pseudopotential in accurately describing the electronic structure. We again performed a G_0W_0 calculation but this time using the SnDjLDAStr pseudopotential and a great improvement was observed, yielding a smaller error of 0.48 eV compared to the experiment and 3 times less than the error due to the SnDjNoCcStr pseudopotential.

Although this represents a significant improvement over SnDjNoCcStr, it underscores the challenges associated with relying solely on the G_0W_0 approximation for accurate band gap predictions.
To address this gap, we performed self-consistent GW calculations using the SnDjLDAStr pseudopotential. This approach provided a much better agreement with the experiment, achieving a band gap only 0.25 eV higher than the experimental value. This result highlights the critical role of self-consistency in GW calculations, which corrects the quasiparticle energies iteratively and mitigates the dependence on the starting point.
The improvement in accuracy achieved with self-consistent GW is attributed to the enhanced treatment of electron-electron interactions and screening effects, which are less accurately captured in a single-shot G_0W_0 calculation. Furthermore, the choice of pseudopotentials proved to be pivotal: the SnDjLDAStr pseudopotential provided better structural and electronic descriptions, leading to closer agreement with the experimental data. The systematic reduction in error from the experimental values, moving from SnDjNoCcStr/G_0W_0 to SnDjLDAStr/$G_0W_0$and finally to SnDjLDAStr/self-consistent GW, demonstrates the necessity of both stringent pseudopotentials of LDA and self-consistency to achieve reliable band gap predictions for SnO_2. These findings emphasize the importance of methodological refinement and suggest that future studies of similar systems should prioritize self-consistent GW calculations with well-constructed pseudopotentials, especially when high accuracy is required.

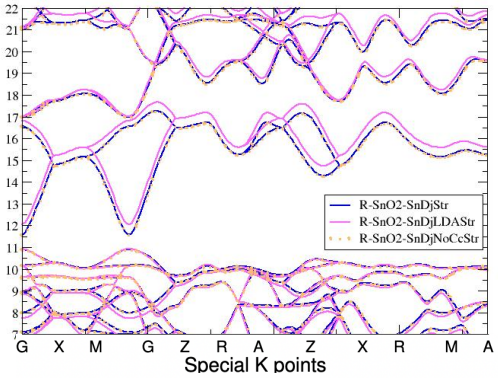

Figure 5.3: Band structure of SnO_2 calculated with SnDjStr, SnDjLDAStr and SnDjNoCcStr pseudopotentials.

Table 5.2: Band gaps for rutile and anatase SnO_2. Rutile direct gap is at Γ and for anatase only the direct band gap is reported.

Material	Methodology	Refs.	E_{Gap}^{DFT}	E_{Gap}^{GW}	ΔE_{Gap}^{GW}
Rutile SnO2	SnDjSta/G_0W_0	This work	0.62	1.58	0.96
Rutile SnO2	SnDjStr/G_0W_0	This work	0.64	1.98	1.34
Rutile SnO2	SnDjNoCcStr/G_0W_0	This work	0.67	2.01	1.34
Rutile SnO2	SnDjLDAStr/G_0W_0	This work	1.13	3.08	1.95
Rutile SnO2	SnDjLDAStr/GW	This work	1.13	3.81	2.68
Rutile SnO2	PP/LDA/G_0W_0	[50]	0.94	2.89	1.95
Rutile SnO2	PP/LDA/G_0W_0	[40]	0.89	2.75	1.86
Rutile SnO2	PP/LDA/G_0W_0	[49]	1.80	3.85	2.05
Rutile SnO2	PP/B3LYP/G_0W_0	[51]	3.5		
Rutile SnO2	PP/HSE/G_0W_0	[52]	3.65		
Rutile SnO2		Exp. [53]		3.56	
Anatase SnO2	SnDjSta	This work	2.30	3.65	1.35

Chapter 6

Conclusions and Perspectives.

In this thesis, we investigated the electronic stucture and quasiparticle energies of TiO_2, IrO_2, and SnO_2 using advanced computational methods. These materials hold significant promise for applications in photocatalysis and photovoltaics because of their unique physical and chemical properties.
The study utilized a combination of DFT and GW to analyze the electronic structures of the materials. The work highlights the following key contributions:

- The electronic band structures of TiO_2, IrO_2, and SnO_2 were computed, showing the need for GW corrections to address the band gap underestimations typical of standard DFT methods (using PBE or LDA). This correction is particularly critical for accurately modeling their performance in photocatalytic and photovoltaic applications.

- The structural and electronic analysis of IrO_2 revealed its complex behavior as a metallic material, highlighting the significant impact of relativistic corrections on its electronic structure. This observation underscores the need for advanced methods, such as the GW beyond Plasmon-Pole Model to fully capture its behavior.

- For SnO_2, the GW approximation provided detailed insights into quasiparticle corrections. These findings enhance the importance of self-consistent GW.

The outcomes of this study deepen the understanding of the fundamental properties of TiO_2, IrO_2, and SnO_2, and also demonstrate the efficacy of combining different computational techniques for material analysis.
The future works could include the calculation of optical properties of SnO_2 in BSE and calculations of quasiparticle energies for IrO_2 but beyond the Plasmon-Pole Model. Moreover, other future work could extend these investigations by exploring the role of the size (clusters and surfaces) and defects or dopants.
In conclusion, this thesis provides a comprehensive understanding of the electronic properties of three key materials, offering valuable insights for their application in the critical domains of photocatalysis and photovoltaics.

Appendix

Table 6.1: Rutile SnO_2 convergence results of BndsRnXp, NGsBlkXp and GbndRnge using SnDjStr pseudopotential.

BndsRnXp	**NGsBlkXp (Ry)**	**GbndRnge**	ΔE_{gap}**(eV)**
100	15	100	1.30859
100	18	100	1.316601
100	21	100	1.321412
100	24	100	1.326048
800	9	800	1.195445
1100	9	1100	1.196192
1300	9	1300	1.196936

Table 6.2: Rutile SnO_2 convergence results of EXXRLvcs and VXCRLvcs using SnDjStr pseudopotential. We used for these calculations : BndsRnXp=1100, NGsBlkXp=21 Ry and GbndRnge=1100.

EXXRLvcs/VXCRLvcs (RL)	ΔE_{gap}**(eV)**
10000	1.33744
15000	1.333864
25000	1.33214
50000	1.331956

Table 6.3: Rutile SnO_2 convergence results of K-Points using SnDjStr pseudopotential. BndsRnXp=500, NGsBlkXp=9 Ry and GbndRnge=500.

K-Points	ΔE_{gap}**(eV)**
557	1.196093
668	1.200019
779	1.202953

Table 6.4: Anatase SnO_2 convergence results of BndsRnXp, NGsBlkXp and GbndRnge using SnDjSta pseudopotential.

BndsRnXp	**NGsBlkXp (Ry)**	**GbndRnge**	ΔE_{gap}**(eV)**
100	15	100	1.50875
100	18	100	1.51321
100	21	100	1.515246
100	24	100	1.516003
800	9	800	1.163322
1100	9	1100	1.167056

Table 6.5: Anatase SnO_2 convergence results of **EXXRLvcs** and **VXCRLvcs** using SnDjSta pseudopotential. We used for these calculations : BndsRnXp=1100, NGsBlkXp=21 Ry and GbndRnge=1100.

EXXRLvcs/VXCRLvcs (RL)	ΔE_{gap}**(eV)**
8000	1.576298
10000	1.57314
15000	1.575092
25000	1.57165
50000	1.569083

Table 6.6: Anatase SnO_2 convergence results of K-Points using SnDjSta pseudopotential. BndsRnXp=500, NGsBlkXp=9 Ry and GbndRnge=500.

K-Points	ΔE_{gap}**(eV)**
553	1.012343
664	1.019788
775	1.02585

Table 6.7: Anatase SnO_2 convergence results of BndsRnXp, NGsBlkXp and GbndRnge using Stringent pseudopotential.

BndsRnXp	**NGsBlkXp (Ry)**	**GbndRnge**	ΔE_{gap}**(eV)**
100	9	100	1.970032
100	12	100	1.987193
100	15	100	2.000422
100	18	100	2.007309
100	21	100	2.011673
100	24	100	2.013983
800	9	800	1.496381
1100	9	1100	1.492461

Table 6.8: Anatase SnO_2 convergence results of **EXXRLvcs** and **VXCRLvcs** using Stringent pseudopotential. We used for these calculations : BndsRnXp=800, NGsBlkXp=21 Ry and GbndRnge=800.

EXXRLvcs/VXCRLvcs (RL)	ΔE_{gap}**(eV)**
8000	1.595253
10000	1.590275
12000	1.591948
15000	1.592242
20000	1.590502

Table 6.9: Anatase SnO_2 convergence results of K-Points using Stringent pseudopotential. BndsRnXp=500, NGsBlkXp=9 Ry and GbndRnge=500.

K-Points	$\mathbf{\Delta E_{gap}(eV)}$
553	1.356662
664	1.362541
775	1.369108

Bibliography

[1] N. Abas, A. Kalair, and N. Khan, "Review of fossil fuels and future energy technologies," *Futures*, vol. 69, pp. 31–49, 2015.

[2] D. Geßner, "Performance of renewable energy policies-evidence from germany's transition to auctions," tech. rep., WEP-Würzburg Economic Papers, 2023.

[3] H. Tong, S. Ouyang, Y. Bi, N. Umezawa, M. Oshikiri, and J. Ye, "Nano-photocatalytic materials: possibilities and challenges," *Advanced materials*, vol. 24, no. 2, pp. 229–251, 2012.

[4] S. Gong and B.-G. Liu, "Electronic structures and optical properties of tio2: Improved density-functional-theory investigation," *Chinese Physics B*, vol. 21, no. 5, p. 057104, 2012.

[5] S. Tingting, Z. Fuchun, and Z. Weihu, "Density functional theory study on the electronic structure and optical properties of sno2," *Rare Metal Materials and Engineering*, vol. 44, no. 10, pp. 2409–2414, 2015.

[6] O. Matz and M. Calatayud, "Periodic dft study of rutile iro2: surface reactivity and catechol adsorption," *The Journal of Physical Chemistry C*, vol. 121, no. 24, pp. 13135–13143, 2017.

[7] A. Pérez-Tomás, A. Mingorance, D. Tanenbaum, and M. Lira-Cantú, "Metal oxides in photovoltaics: all-oxide, ferroic, and perovskite solar cells," in *The future of semiconductor oxides in next-generation solar cells*, pp. 267–356, Elsevier, 2018.

[8] J. Houska, S. Mraz, and J. Schneider, "Experimental and molecular dynamics study of the growth of crystalline tio2," *Journal of Applied Physics*, vol. 112, no. 7, 2012.

[9] A. Fujishima and K. Honda, "Electrochemical photolysis of water at a semiconductor electrode," *nature*, vol. 238, no. 5358, pp. 37–38, 1972.

[10] M. Grätzel, "Photoelectrochemical cells," *nature*, vol. 414, no. 6861, pp. 338–344, 2001.

[11] F. Grant, "Properties of rutile (titanium dioxide)," *Reviews of Modern Physics*, vol. 31, no. 3, p. 646, 1959.

[12] U. Diebold, "The surface science of titanium dioxide," *Surface science reports*, vol. 48, no. 5-8, pp. 53–229, 2003.

[13] D. Reyes-Coronado, G. Rodríguez-Gattorno, M. Espinosa-Pesqueira, C. Cab, R. De Coss, and G. Oskam, "Phase-pure tio2 nanoparticles: anatase, brookite and rutile," *Nanotechnology*, vol. 19, no. 14, p. 145605, 2008.

[14] A. Soussi, A. Ait Hssi, M. Boujnah, L. Boulkadat, K. Abouabassi, A. Asbayou, A. Elfanaoui, R. Markazi, A. Ihlal, and K. Bouabid, "Electronic and optical properties of tio2 thin films: combined experimental and theoretical study," *Journal of Electronic Materials*, vol. 50, no. 8, pp. 4497–4510, 2021.

[15] B. O'regan and M. Grätzel, "A low-cost, high-efficiency solar cell based on dye-sensitized colloidal tio2 films," *nature*, vol. 353, no. 6346, pp. 737–740, 1991.

[16] H. Yan, X. Wang, M. Yao, and X. Yao, "Band structure design of semiconductors for enhanced photocatalytic activity: The case of tio2," *Progress in Natural Science: Materials International*, vol. 23, no. 4, pp. 402–407, 2013.

[17] S. Trasatti, "Electrodes of conductive metallic oxides," *(No Title)*, 1980.

[18] Y. S. Jin, K. H. Kim, S. J. Park, H. H. Yoon, and H. W. Choi, "Nanostructured tio2 films for dye-sensitized solar cells prepared by the sol–gel method," *Journal of Nanoscience and Nanotechnology*, vol. 11, no. 12, pp. 10971–10975, 2011.

[19] J. Mistrik, S. Kasap, H. E. Ruda, C. Koughia, and J. Singh, "Optical properties of electronic materials: fundamentals and characterization," *Springer handbook of electronic and photonic materials*, pp. 1–1, 2017.

[20] L. Hedin, "New method for calculating the one-particle green's function with application to the electron-gas problem," *Physical Review*, vol. 139, no. 3A, p. A796, 1965.

[21] M. Rohlfing and S. G. Louie, "Electron-hole excitations and optical spectra from first principles," *Physical Review B*, vol. 62, no. 8, p. 4927, 2000.

[22] G. Onida, L. Reining, and A. Rubio, "Electronic excitations: density-functional versus many-body green's-function approaches," *Reviews of modern physics*, vol. 74, no. 2, p. 601, 2002.

[23] W. G. Aulbur, L. Jnsson, and W. John, "Wilkins. quasiparticle calculations in solids. volume 54 of solid state physics," 1999.

[24] L. Reining, "The gw approximation: content, successes and limitations," *Wiley Interdisciplinary Reviews: Computational Molecular Science*, vol. 8, no. 3, p. e1344, 2018.

[25] C. Friedrich and A. Schindlmayr, "Many-body perturbation theory: The gw approximation," in *Computational Nanoscience: Do It Yourself!* (J. Grotendorst, S. Blügel, and D. Marx, eds.), vol. 31 of *NIC Series*, pp. 335–355, John von Neumann Institute for Computing, Jülich, 2006.

[26] P. Hohenberg and W. Kohn, "Inhomogeneous electron gas," *Physical review*, vol. 136, no. 3B, p. B864, 1964.

[27] L. J. Bartolotti and K. Flurchick, "An introduction to density functional theory," *Reviews in computational chemistry*, pp. 187–216, 1996.

[28] W. Kohn and L. J. Sham, "Self-consistent equations including exchange and correlation effects," *Physical review*, vol. 140, no. 4A, p. A1133, 1965.

[29] C. A. Adessi, "Introduction to density functional theory (dft)." https://ilm-perso.univ-lyon1.fr/~cadessi/Doc/ab_initio_lecture.pdf, 2024. Accessed: 2024-10-28.

[30] F. Bruneval, "Exchange and correlation in the electronic structure of solids, from silicon to cuprous oxide: Gw approximation and beyond," *PhD Thesis*, 2005.

[31] J. P. Perdew, K. Burke, and M. Ernzerhof, "Generalized gradient approximation made simple," *Physical review letters*, vol. 77, no. 18, p. 3865, 1996.

[32] C. Friedrich and A. Schindlmayr, "Many-body perturbation theory: The gw approximation," *NIC Series*, vol. 31, p. 335, 2006.

[33] D. Sangalli, A. Ferretti, H. Miranda, C. Attaccalite, E. Cannuccia, P. Melo, M. Marsili, F. Paleari, I. Marri, D. Varsano, *et al.*, "Yambo: An ab initio tool for excited state calculations," *Journal of Physics: Condensed Matter*, vol. 31, no. 32, p. 325902, 2019.

[34] P. Schwerdtfeger, "The pseudopotential approximation in electronic structure theory," *ChemPhysChem*, vol. 12, no. 17, pp. 3143–3155, 2011.

[35] E. Luppi, H.-C. Weissker, S. Bottaro, F. Sottile, V. Veniard, L. Reining, and G. Onida, "Accuracy of the pseudopotential approximation in ab initio theoretical spectroscopies," *Phys. Rev. B*, vol. 78, p. 245124, Dec 2008.

[36] D. R. Hamann, "Optimized norm-conserving vanderbilt pseudopotentials," *Phys. Rev. B*, vol. 88, p. 085117, Aug 2013.

[37] D. A. Leon, A. Ferretti, D. Varsano, E. Molinari, and C. Cardoso, "Efficient full frequency gw for metals using a multipole approach for the dielectric screening," *Phys. Rev. B*, vol. 107, p. 155130, Apr 2023.

[38] W. O. University, "Periodic table of the elements downloadable version." https://wou.edu/chemistry/files/2017/04/Periodic-Table-Downloadable-Version.pdf, 2017. Accessed: 2024-11-02.

[39] and , "Electronic structures and optical properties of tio_2: Improved density-functional-theory investigation," *B:* , vol. 21, no. 5, pp. 508–514, 2012.

[40] A. Miglio, R. Saniz, D. Waroquiers, M. Stankovski, M. Giantomassi, G. Hautier, G.-M. Rignanese, and X. Gonze, "Computed electronic and optical properties of sno2 under compressive stress," *Optical Materials*, vol. 38, pp. 161–166, 2014.

[41] L. Chiodo, J. M. García-Lastra, A. Iacomino, S. Ossicini, J. Zhao, H. Petek, and A. Rubio, "Self-energy and excitonic effects in the electronic and optical properties of tio 2 crystalline phases," *Physical Review B—Condensed Matter and Materials Physics*, vol. 82, no. 4, p. 045207, 2010.

[42] B. Hamad, "First-principle calculations of structural and electronic properties of rutile-phase dioxides (mo 2), m= ti, v, ru, ir and sn," *The European Physical Journal B*, vol. 70, pp. 163–169, 2009.

[43] A. A. Bolzan, C. Fong, B. J. Kennedy, and C. J. Howard, "Structural studies of rutile-type metal dioxides," *Acta Crystallographica Section B: Structural Science*, vol. 53, no. 3, pp. 373–380, 1997.

[44] L. G. Ferreira, M. Marques, and L. K. Teles, "Approximation to density functional theory for the calculation of band gaps of semiconductors," *Physical Review B—Condensed Matter and Materials Physics*, vol. 78, no. 12, p. 125116, 2008.

[45] A. Guandalini, P. D'Amico, A. Ferretti, and D. Varsano, "Efficient gw calculations in two dimensional materials through a stochastic integration of the screened potential," *npj Computational Materials*, vol. 9, p. 44, Mar 2023.

[46] A. Schleife, J. B. Varley, F. Fuchs, C. Rödl, F. Bechstedt, P. Rinke, A. Janotti, and C. G. Van de Walle, "Tin dioxide from first principles: Quasiparticle electronic states and optical properties," *Physical Review B*, vol. 83, p. 035116, Jan 2011.

[47] J. Mazumder, R. Mayengbam, and S. Tripathy, "Theoretical investigation on structural, electronic, optical and elastic properties of tio2, sno2, zro2 and hfo2 using scan meta-gga functional: A dft study," *Materials Chemistry and Physics*, p. 123474, 06 2020.

[48] J. Haines and J. Léger, "X-ray diffraction study of the phase transitions and structural evolution of tin dioxide at high pressure: ffrelationships between structure types and implications for other rutile-type dioxides," *Physical Review B*, vol. 55, no. 17, p. 11144, 1997.

[49] R. Saniz, H. Dixit, D. Lamoen, and B. Partoens, "Quasiparticle energies and uniaxial pressure effects on the properties of sno," *Applied Physics Letters*, vol. 97, no. 26, p. 261901, 2010.

[50] J. A. Berger, L. Reining, and F. Sottile, "Efficient *gw* calculations for sno_2, zno, and rubrene: The effective-energy technique," *Phys. Rev. B*, vol. 85, p. 085126, Feb 2012.

[51] F. Trani, M. Causà, D. Ninno, G. Cantele, and V. Barone, "Density functional study of oxygen vacancies at the sno surface and subsurface sites," *Physical Review B*, vol. 77, no. 24, p. 245410, 2008.

[52] A. Schleife and F. Bechstedt, "Ab initio description of quasiparticle band structures and optical near-edge absorption of transparent conducting oxides," *Journal of Materials Research*, vol. 27, no. 17, pp. 2180–2189, 2012.

[53] D. Fröhlich, R. Kenklies, and R. Helbig, "Band-gap assignment in sno by two-photon spectroscopy," *Physical Review Letters*, vol. 41, no. 25, pp. 1750–1751, 1978.